

Oceanic Fronts Driven by the Amazon Freshwater Plume and Their Thermohaline Compensation at the Submesoscale



Key Points:

- Vertical shear sections from the Sailldroné ADCP data reveal that temperature compensation develops along restratifying submesoscale fronts
- Temperature and salinity spectra show an increased temperature contribution to salinity-dominated fronts at the submesoscale
- A flattening of the density spectra from ~ -3 to ~ -2 at the submesoscale (1–10 km) is observed in the Boulevard des Tourbillons

Supporting Information:

Supporting Information may be found in the online version of this article.

Correspondence to:

S. Coadou-Chaventon,
solange.coadou-chaventon@lmd.ipsl.fr

Citation:

Coadou-Chaventon, S., Speich, S., Zhang, D., Rocha, C. B., & Swart, S. (2024). Oceanic fronts driven by the Amazon freshwater plume and their thermohaline compensation at the submesoscale. *Journal of Geophysical Research: Oceans*, 129, e2024JC021326. <https://doi.org/10.1029/2024JC021326>

Received 21 MAY 2024

Accepted 28 JUN 2024

Author Contributions:

Conceptualization: S. Coadou-Chaventon, S. Speich, S. Swart

Data curation: D. Zhang, C. B. Rocha

Formal analysis: S. Coadou-Chaventon

Investigation: S. Coadou-Chaventon, S. Speich, S. Swart

Methodology: S. Coadou-Chaventon, S. Speich, S. Swart

Resources: D. Zhang, C. B. Rocha

Supervision: S. Speich, S. Swart

Writing – original draft: S. Coadou-Chaventon

Writing – review & editing: S. Coadou-Chaventon, S. Speich, D. Zhang, C. B. Rocha, S. Swart

Writing – review & editing: S. Coadou-Chaventon, S. Speich, D. Zhang, C. B. Rocha, S. Swart

Writing – review & editing: S. Coadou-Chaventon, S. Speich, D. Zhang, C. B. Rocha, S. Swart

Writing – review & editing: S. Coadou-Chaventon, S. Speich, D. Zhang, C. B. Rocha, S. Swart

Writing – review & editing: S. Coadou-Chaventon, S. Speich, D. Zhang, C. B. Rocha, S. Swart

Writing – review & editing: S. Coadou-Chaventon, S. Speich, D. Zhang, C. B. Rocha, S. Swart

Writing – review & editing: S. Coadou-Chaventon, S. Speich, D. Zhang, C. B. Rocha, S. Swart

Writing – review & editing: S. Coadou-Chaventon, S. Speich, D. Zhang, C. B. Rocha, S. Swart

Writing – review & editing: S. Coadou-Chaventon, S. Speich, D. Zhang, C. B. Rocha, S. Swart

Writing – review & editing: S. Coadou-Chaventon, S. Speich, D. Zhang, C. B. Rocha, S. Swart

Writing – review & editing: S. Coadou-Chaventon, S. Speich, D. Zhang, C. B. Rocha, S. Swart

Writing – review & editing: S. Coadou-Chaventon, S. Speich, D. Zhang, C. B. Rocha, S. Swart

Writing – review & editing: S. Coadou-Chaventon, S. Speich, D. Zhang, C. B. Rocha, S. Swart

Writing – review & editing: S. Coadou-Chaventon, S. Speich, D. Zhang, C. B. Rocha, S. Swart

Writing – review & editing: S. Coadou-Chaventon, S. Speich, D. Zhang, C. B. Rocha, S. Swart





Writing – review & editing: S. Coadou-Chaventon, S. Speich, D. Zhang, C. B. Rocha, S. Swart

Writing – review & editing: S. Coadou-Chaventon, S. Speich, D. Zhang, C. B. Rocha, S. Swart

Writing – review & editing: S. Coadou-Chaventon, S. Speich, D. Zhang, C. B. Rocha, S. Swart

Writing – review & editing: S. Coadou-Chaventon, S. Speich, D. Zhang, C. B. Rocha, S. Swart

Writing – review & editing: S. Coadou-Chaventon, S. Speich, D. Zhang, C. B. Rocha, S. Swart

S. Coadou-Chaventon^{1,2} , S. Speich¹ , D. Zhang³, C. B. Rocha⁴ , and S. Swart^{2,5} 

¹LMD/IPSL, ENS, École Polytechnique, Institut Polytechnique de Paris, PSL University, Sorbonne Université, CNRS, Paris, France, ²Department of Marine Sciences, University of Gothenburg, Gothenburg, Sweden, ³National Oceanic and Atmospheric Administration (NOAA), Pacific Marine Environmental Laboratory (PMEL), CICOES, University of Washington, Seattle, WA, USA, ⁴Instituto Oceanográfico, Universidade de São Paulo, São Paulo, Brazil, ⁵Department of Oceanography, University of Cape Town, Rondebosch, South Africa

Abstract Upper ocean fronts are dynamically active features of the global ocean playing a key role in the air-sea exchanges of properties and their transport in the ocean interior. With scales ranging from the submesoscale (0.1–10 km) to the mesoscale (10–100s km) and a temporal variability from hours to months, collecting in situ observations of these structures is challenging and this has limited our understanding of their associated processes and impacts. During the EUREC4A-OA/ATOMIC field experiment, which took place in the northwest tropical Atlantic in January–February 2020, a large number of uncrewed platforms, including five Sailldrones, were deployed to provide a detailed picture of the upper-ocean fine-scale variability. This region is strongly influenced by the outflow of the Amazon River, even in winter, which is the minimum outflow season. Here, the generation of fine-scale horizontal thermohaline gradients is driven by the stirring of this freshwater river input by large anticyclonic eddies, the so-called North Brazil Current Rings. Vertical shear estimates using the Sailldrones ADCP show that partial temperature compensation occurs along restratifying submesoscale salinity-dominated fronts. The distribution of surface along-track gradients, as sampled by different horizontal length-scales, reveals the prevalence of submesoscale fronts. This is supported by a flattening of the spectral slopes of surface density at the submesoscale. This study emphasizes the need to resolve the upper ocean at high spatial resolution to understand its impact on the broader circulation and to properly represent air-sea interactions.

Plain Language Summary Oceanic eddies and filaments that range between 10 and 100 km in size can be identified in the study region of the northwestern tropical Atlantic using ocean color as viewed from space (a proxy for chlorophyll-*a*). The ocean color maps show that these eddies and filaments are associated with the detachment from the shelf of a freshwater Amazon plume and its interaction with the larger oceanic motions $\mathcal{O}(100$ km). Field observations from different measurements acquired from research vessels and five uncrewed surface vehicles (USVs) reveal the prevalence and scale of upper ocean fronts, whose magnitude results from the combined effect of temperature and salinity. The Amazon freshwater plume is key to the formation of strong salinity-driven density fronts. However, when looking at $\mathcal{O}(1$ km) scales, we detect horizontal temperature variations along slumping fronts that partially counteract the effect of salinity. This leads to a damping of the lateral density fronts. This study contributes to the development of a detailed picture of the ocean fine scales, which is necessary to improve our understanding of air-sea interactions over frontal regions.

1. Introduction

Submesoscale fronts in the upper ocean contribute significantly to the vertical transport of climate properties, such as heat, moisture or CO₂, across the pycnocline. Both numerical (Su et al., 2020) and in situ (Siegelman et al., 2020) studies show that they are associated with intense vertical velocities that provide a dynamical conduit connecting the upper ocean with the interior and the different interfaces: the marginal ice zone (Biddle & Swart, 2020; Manucharyan & Thompson, 2017) and the atmospheric boundary layer (Small et al., 2008; Wenegrat & Arthur, 2018). They strongly affect the mixed layer (ML) properties on a timescale of days by transferring the forcing at these interfaces into the stratified interior, changing properties of the upper pycnocline and the stratification through baroclinic instability and eddies that convert potential energy into kinetic energy (Boccaletti et al., 2007; Fox-Kemper et al., 2008). While the contribution of submesoscale and fine-scale fronts to vertical fluxes of buoyancy, heat, gases and nutrients (Lévy et al., 2012; Meroni et al., 2018) has started to be

© 2024. The Author(s).

This is an open access article under the terms of the [Creative Commons Attribution License](https://creativecommons.org/licenses/by/4.0/), which permits use, distribution and reproduction in any medium, provided the original work is properly cited.

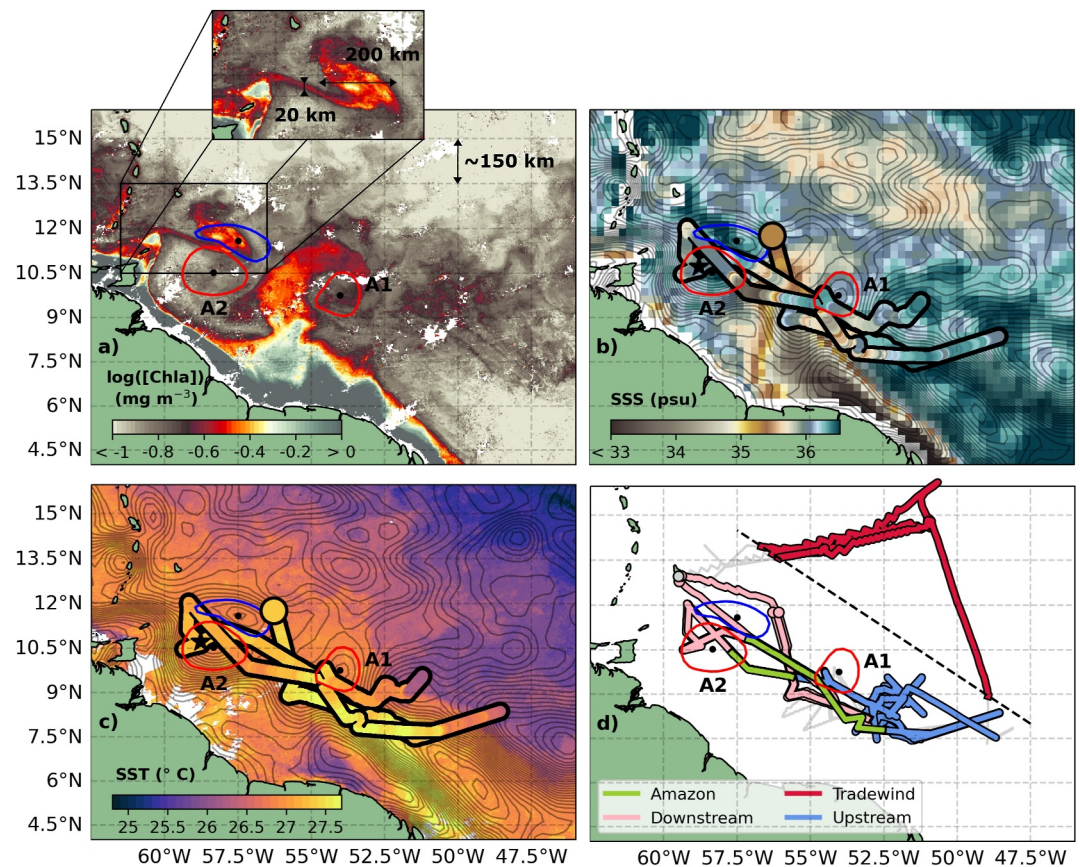


Figure 1. Satellite maps of (a) Chl-*a*, (b) SSS and (c) SST on 12 February 2020. (d): Trajectories of the five SAILDRONES color-coded with the regions (Amazon (green), Downstream (pink), Tradewind (red) and Upstream (blue)). The light gray line indicates unused data from SAILDRONE 1064. Eddy contours are derived from the TOEddies eddy detection and tracking algorithm (Laxenaire et al., 2018) applied to Maps of Absolute Dynamic Topography (MADT): light gray contours in (b)–(d), red contours for anticyclones, blue contours for cyclones. The trajectory of SAILDRONE 1026 is color-coded by in situ measurements of (b) salinity and (c) temperature. Its position at the time closest to the satellite map is indicated by a black star. In (b)–(d), the start of the measurement period of each SAILDRONE is shown by a circle. A zoom in (a) highlights some of the mesoscale and submesoscale features tracked by the Chl-*a* concentration. Some length scales are shown in (a). In (d), the dashed black line shows the separation between the Boulevard des Tourbillons and the Tradewind Alley.

considered, their magnitude and distribution remain poorly documented. No consistency exists in the literature regarding the definition of submesoscales. While Su et al. (2020) refer to scales smaller than 0.5° (~ 50 km) as submesoscales, Biddle and Swart (2020) use the Rossby deformation radius as the cutoff between meso- and submesoscale. For the purposes of this study, we define submesoscale fronts and eddies as having a spatial scale of $\mathcal{O}(0.1\text{--}10$ km), which is consistent with the definition by Swart et al. (2023).

Oceanic fronts exhibit sharp temperature, salinity and/or biological gradients as they correspond to the transition zone between water masses with different physical and chemical properties. These gradients occur on scales ranging from thousands of kilometers down to millimeters and are linked by a horizontal and vertical down-scale variance cascade (Smith & Ferrari, 2009). The surface imprint of submesoscale and mesoscale fronts has been revealed by remotely sensed data suggesting that they are ubiquitous (Dong & Zhong, 2020; Mauzole, 2022). In particular, ocean color products such as chlorophyll-*a* (Chl-*a*) reveal the submesoscale structuring of fronts, filaments, meanders and eddies at scales of $\mathcal{O}(1\text{--}10$ km) (Figure 1a). As density is temperature controlled in most of the world's upper ocean (Johnson et al., 2012), sea surface temperature (SST) maps are useful illustrations of the ocean dynamics down to the same range of scales. If frontal studies have been relying on these satellite products historically (Simpson, 1981), they can only tell part of the story of frontal dynamics as ocean color is a nonconservative tracer and temperature may be salinity-compensated (Rudnick & Martin, 2002).

For regions experiencing intense freshwater runoff, rainfall or sea ice melt, sea surface salinity (SSS) may even be the parameter of interest. However, the L-band satellite radiometry from which SSS is derived cannot resolve the fine-scale structures (Boutin et al., 2016). Any freshwater or saline anomaly on the SSS maps slowly fades away as the initial salinity gradients are stirred and sharpened by large-scale motions such as currents, mesoscale eddies, instabilities and internal waves, resulting in small-scale fronts that are not resolved by the product resolution of the satellites (40–100 km). This observational gap regarding the cascade of SSS anomalies from the large-scale to sufficiently small scales, where isotropic turbulence and molecular diffusion ultimately mix properties and dissipate tracer gradients (Shcherbina et al., 2015), leaves unanswered questions about the resulting submesoscale fronts. Even high-resolution satellite data cannot resolve scales below $\mathcal{O}(0.1$ km), which has limited our understanding of fine-scale processes (Chapron et al., 2020). In addition, the regime of submesoscale dynamics that connects the larger mesoscale to the smaller dissipative scales, operates on timescales down to a few days to hours (McWilliams, 2016), which is too short to be captured by the gridded satellite products with a usual 1-week time averaging. Global observational efforts to resolve the rapidly evolving dynamics of the ocean fine-scale are rapidly advancing, with the development and deployment of high-resolution autonomous observing platforms such as Uncrewed Surface Vehicles (USVs) and underwater gliders, and high-resolution ship-based surveys using closely spaced hydrographic stations or towed instruments.

In recent years, these technological capabilities have provided valuable data sets that reveal fine-scale variability and contribute to our understanding of submesoscale dynamics in the world ocean. These new data sets provide observational evidence for the role of submesoscale processes in ML stratification in different ocean basins: the North Atlantic (Mahadevan et al., 2012; Thompson et al., 2016) and the Southern Ocean (Du Plessis et al., 2017, 2019). These observing platforms have also proven to be able to make accurate measurements (Zhang et al., 2019) in coastal areas (Vazquez-Cuervo et al., 2019) and at high latitudes (Chiodi et al., 2021) which are regions lacking in situ observations and where SSS products still present some inaccurate measurements (Köhler et al., 2015), while being particularly relevant to society.

Fine-scale horizontal variability has been studied since the late 1990s prior to the development of these platforms. In subtropical gyres, horizontal density variability at the ocean surface was found to be limited to scales above 10 km despite the presence of large and sharp surface thermohaline fronts below this scale (North Pacific—Rudnick & Ferrari, 1999; Rudnick & Martin, 2002). However, the collection of data from different seasons shows that compensation may not be found in summer when the ML is shallow and thus vertical mixing is reduced (North Atlantic—Kolodziejczyk et al., 2015). In the Bay of Bengal, which is characterized by large freshwater inputs, Spiro Jaeger and Mahadevan (2018) observed that large-scale salinity-driven density fronts tend to compensate at the scale of frontal restratification. Using a process study model, they show that small-scale temperature and salinity coherence is the result of enhanced surface cooling of the shallower and less saline surface mixed layer. These elements suggest that horizontal thermohaline structures may be subject to very different spatiotemporal behaviors given the ML variability, which is modulated—among many processes—by the seasonal cycle of surface heat fluxes and external forcings such as freshwater inputs or sea ice melt.

The Northwestern Tropical Atlantic is a well-suited natural laboratory for studying horizontal surface density gradients over a wide range of scales. This region is strongly influenced by the outflow of the Amazon River, which is unique in its magnitude. It accounts for nearly 20% of the global river freshwater input to the ocean, which is no less than the combined discharge of the next seven largest rivers in the world (Dai & Trenberth, 2002). This freshwater input contrasts with the more saline and warm water advected across the equator by the North Brazil Current (NBC), creating large-scale density fronts. From June to January, the NBC turns back on itself in a tight loop known as the NBC retroflection (Richardson & Walsh, 1986; Schott et al., 1998), which occasionally spawns some of the world's largest eddies (Richardson et al., 1994), commonly referred to as NBC rings. These anticyclonic eddies travel northward along the coast within the Boulevard des Tourbillons (Fratantoni & Glickson, 2002), a warm corridor that contrasts with the colder waters of the open ocean (Figure 1c), a region named the Tradewind Alley after the dominant winds (Stevens et al., 2021), which is also known to be much less spatially variable. The fate and dispersal of this freshwater have been analyzed from satellite data using the ocean color signature of the Amazon (Hu et al., 2004), revealing the role of NBC rings in entraining these fresh waters from the shelf-break to the open ocean (Olivier et al., 2022; Reverdin et al., 2021). This is of particular interest given the role of fresher surface layers in promoting the development of barrier layers and temperature inversions at the base of the halocline (Mignot et al., 2012). Several studies in the vicinity of the Amazon plume region have shown that barrier layers increase the resistance of the upper ocean to cooling, keeping it warmer and supporting

Table 1

For Each Saildrone Data Set: Operating Period, Sampling Frequency and Associated Spatial Resolution As Well As the Mean and Standard Deviation Difference (STD) Between Saildrone and Satellite Data

| Name | Operating period (days) | Temporal resolution (min) | Spatial resolution $\mu \pm \sigma$ (m) | Saildrone – satellite | | | |
|--------|-------------------------|---------------------------|---|-----------------------|-------|-----------|-------|
| | | | | SST (°C) | | SSS (psu) | |
| | | | | Mean | STD | Mean | STD |
| SD1026 | 01-17-20–03-03-20 (47) | 1 | 85 ± 31 | 0.339 | 0.227 | −0.264 | 0.268 |
| SD1060 | 01-17-20–03-03-20 (47) | 1 | 85 ± 30 | 0.340 | 0.246 | −0.278 | 0.275 |
| SD1061 | 01-17-20–03-03-20 (47) | 1 | 87 ± 30 | 0.339 | 0.217 | −0.269 | 0.257 |
| SD1063 | 01-13-20–03-08-20 (56) | 1 | 88 ± 30 | 0.312 | 0.220 | −0.268 | 0.239 |
| SD1064 | 01-17-20–04-11-20 (86) | 5 | 392 ± 144 | 0.278 | 0.230 | −0.148 | 0.375 |

hurricane intensification (Androulidakis et al., 2016; Ffield, 2007). Therefore, understanding the dispersion processes of the Amazon plume seems essential to get an accurate picture of the SSS pattern in the northwestern tropical Atlantic, given its role in setting the weather and climate extremes to which the Caribbean nations are vulnerable.

The deployment of different observing platforms from four ships and five Saildrones during the EUREC4A-OA/ATOMIC experiment (Stevens et al., 2021; Quinn et al., 2021) in winter 2020 supported the investigation of mesoscale and submesoscale sea surface thermohaline variability in the northwestern tropical Atlantic. In this work we investigate regional contrasts in submesoscale activity and associated fronts related to the northwestward advection of a freshwater plume. We use data from the five Saildrones, which have sampled a large region, including the Boulevard des Tourbillons and the Trade Wind Alley, combined with vertical profiles acquired by the ships and other uncrewed platforms, satellite data and reanalysis products. Acoustic Doppler Current Profiler (ADCP) data from the Saildrones are used to gain insight into the mixed layer depth and shear, and provide evidence for temperature compensation that is generated along restratifying submesoscale fronts. A wavelet analysis is carried to statistically support these observations. Thermohaline gradient distributions and spectra are computed to address the role of freshwater forcing on frontogenesis and the prevalence of submesoscale fronts.

2. Data and Methods

2.1. In Situ Data

2.1.1. Saildrones Data

During the EUREC4A-OA/ATOMIC cruise, five Saildrones—three NASA-funded (SD1026, SD1060, SD1061) and two NOAA-funded (SD1063, SD1064)—were deployed. Saildrones navigate within a sailing corridor through a set of remotely prescribed waypoints. They were updated by scientists during the cruise to capture the evolution of the features of interest using near real-time satellite observations. The Saildrones measured surface salinity and temperature using a pumped SeaBird-37-SMP-ODO Microcat CTD at 0.5 m depth. A 300 kHz ADCP was mounted on the keel and measured upper ocean velocity profiles between 6 and 100 m depth, at 2 m intervals. Onboard data processing with real-time motion correction provided 1-min data averages (5-min averages for ADCP measurements) that were transmitted in real-time. Specifically for SD1064, surface T and S were only measured for 1 min at every 5-min intervals in order to preserve the antifouling agent in the pumped CTD for an extended deployment.

The Saildrones were deployed off the southern coast of Barbados. The three NASA Saildrones and SD1063 monitored the Boulevard des Tourbillons ocean eddy corridor southeast of Barbados, during 47 and 56 days, respectively. Using 1-min averages, they mapped the ocean surface at an average horizontal spatial scale of 86 m (Table 1). SD1064 crossed both the Boulevard des Tourbillons and the Tradewind Alley for 86 days, with 1-min averages every 5 min, corresponding to an horizontal resolution of 392 ± 144 m. The different path taken by SD1064 is highlighted by the comparison with satellite data, with a lower mean difference for both SST and SSS products for SD1064 despite a higher standard deviation difference for SSS (Table 1). Overall, all Saildrones

observations were fresher than SSS satellite data, pointing out the misrepresentation of the freshwater plume and coastal waters in SSS maps.

This study aims to investigate the spatial variability of the ocean surface thermohaline properties, so the Saildrones time series are treated as snapshots in time. However, the temporal and spatial components cannot be separated when calculating the gradients along the track. The lateral temperature and salinity gradients crossed by the Saildrones may contain components of temporal variability, such as temporal changes to heat and freshwater forcing. We have assessed available evidence for the low temporal variability in the data sets. In particular, to determine the amplitude of the diurnal cycle, we applied a Singular Spectral Analysis on the Saildrones SST time series, which allowed us to recover a space-time varying diurnal cycle.

The estimated variance of each mode as a function of its corresponding frequency revealed that the pair of principal components representing the diurnal cycle account for only a small fraction of the total variance (less than 1%) (Figure S1b in Supporting Information S1). The reconstructed diurnal cycle was built from the selected principal components and showed a diurnal signal with an amplitude no greater than 0.15°C (Figure S1a in Supporting Information S1). Additionally, several Saildrones followed parallel tracks with a time lag (Figure 1d), allowing direct insight into the magnitude of the temporal versus spatial variability (Figure S2 in Supporting Information S1). It was found that the strongest features remain consistent over time from 2 to 12hr. Table 1 shows that minimum speed of the Saildrones is 3 km hr⁻¹ suggesting that temporal variability has negligible effect on scales up to 30–36 km. This work focuses mainly on spatial variability at scales below 50 km, for which we postulate that temporal variability (over ~16 hr) has little influence on the total observed variability. Therefore, in this study we assume that surface horizontal thermohaline gradients are dominated by spatial features.

2.1.2. Auxiliary In Situ Observations

Saildrones only measure surface hydrographic properties, leaving questions about the underlying stratification unanswered. To provide further insight into the stratification in the upper layers of the water column, high quality vertical profiles collected by Conductivity Temperature and Depth (CTD) sensors deployed from the research vessels, underway CTDs (uCTD), Gliders, Moving Vessel Profilers (MVP), Argo floats and Underwater Gliders were used. This was made possible by the large observing capacity of the EUREC4A-OA/ATOMIC campaign, including both a wide variety of observing platforms and a large number of measurements collected from the four participating research vessels (RVs): RV L'Atalante (Speich & The Embarked Science Team, 2021), RV Maria S. Merian (Karstensen et al., 2020), RV Ronald H. Brown (Quinn et al., 2021) and RV Meteor. All the data have been calibrated and cross-validated against 120 quality-controlled CTD profiles to ensure consistency between data sets from all platforms (L'Hégaret et al., 2023).

2.2. Satellite and Reanalysis Data

Satellite data of different properties provide the appropriate synoptic tool to gain insight into the surface dynamics of the region at the time of the EUREC4A-OA/ATOMIC experiment. We analyzed daily maps of SSS, SST, Chl-*a* concentration and MADT to contextualize the Saildrones measurements in terms of the ocean dynamics from 2D surface fields. We used the 70-km mapped salinity product from the Soil Moisture Active Passive product processed by the Remote Sensing System (SMAP RSS). It is produced on a 0.25° grid with an 8-day running mean. From the analysis of four different salinity products, it was found to be the one most consistent with the salinity values recorded by the Saildrones (Hall et al., 2022). Since the European product Soil Moisture Ocean Salinity (SMOS) (Boutin et al., 2018) was not included in the comparison, it was briefly examined. The SMAP RSS product is smoother than SMOS but their small differences were not significant for this study. SST and Chl-*a* concentration maps are produced by CLS on a 0.02° grid (Olivier et al., 2022; Reverdin et al., 2021; Stum et al., 2015). MADT data on a 0.25° grid are used to provide an indication of the surface geostrophic currents. Produced by Ssalto/Duacs and distributed by the Copernicus Marine Environment Monitoring Service (CMEMS), they result from the combination of all the data recorded by the satellites available under the different altimetric missions. The TOEddies algorithm developed by Laxenaire et al. (2018) was run to identify eddies and to detect when Saildrones intersected one.

ERA5 reanalysis data (Hersbach et al., 2021) have been used to estimate the net heat flux along the trajectory of the Saildrones. Hourly estimates provided on a regular lat-lon grid of 0.25° were used for net shortwave radiation, net longwave radiation, sensible heat, and latent heat flux.

2.3. Wavelet Analysis

To address the relative contribution of lateral temperature and salinity gradients to the magnitude of the density gradients along the track over a wide range of scales, the density ratio was estimated:

$$R = \frac{\alpha \Delta T}{\beta \Delta S} \quad (1)$$

where α , β are the thermal expansion and haline contraction coefficients, respectively, and ΔT , ΔS are the horizontal variations of T and S along the Saildrone track at different scales. Following previous studies, a wavelet analysis is performed to evaluate ΔT and ΔS (Kolodziejczyk et al., 2015; Rudnick & Ferrari, 1999; Spiro Jaeger & Mahadevan, 2018). It has been shown that the wavelet transform method is particularly well suited for frontal phenomena analysis compared to Fourier and EOF analysis (Gamage & Blumen, 1993) as it provides a space scale decomposition.

Each T and S time series is converted from a time-based measurement to a spatial measurement with constant spacing ($\Delta x = 0.4$ km, the coarser spatial resolution of the Saildrones data set—Table 1) by linear interpolation and a continuous wavelet transform is performed (for more details, see Torrence & Compo, 1998). By using the wavelet coefficients of T and S derived from this computation as estimates of ΔT and ΔS and multiplying them by the space dependent thermal expansion and haline contraction coefficients, respectively, a space and scale dependent density ratio can be estimated. Since the wavelet coefficients of T and S are complex numbers, we retrieve a complex density ratio which can thus be written as $|R| e^{i\phi}$. Its phase ϕ is a measure of T and S coherence with $\phi = 0$ ($\phi = 180$) when T and S gradients reduce (strengthen) the density variation. Its modulus $|R|$ indicates the relative strength of T and S gradients. Despite its more intuitive interpretation, the analysis of $|R|$ is performed by looking at the quantity $\arctan |R|$ since it is bounded between 0 and $\frac{\pi}{2}$ while $|R|$ has an infinite range and the temperature-dominated regions ($1 < |R| < \infty$) occupy the same space on the arctan scale as the salinity-dominated regions ($0 < |R| < 1$).

3. Results

3.1. Observational Evidence of Fine-Scale Structures

3.1.1. From Remote Observations

High resolution Chl-*a* satellite maps highlight the presence of sub-mesoscale eddies and filaments with lateral width of $\mathcal{O}(10$ km) (Figures 1a and 2d–2f) during the EUREC4A/ATOMIC campaign, indicating that the region is characterized by intense frontal activity. At the beginning of the Saildrones sampling period (Figure 2d) in January 2020, the high chlorophyll concentrations appeared mostly at the edge of mesoscale eddies and along the North Brazil Current Retroflection and resulted from the stirring of shelf waters by the latter. In early February, the larger Chl-*a* signal observed along $\sim 55^\circ$ W (Figure 2e) coincided with the detachment of a freshwater plume from the Guiana Plateau (Figure 1b). The transport of highly productive waters into nutrient-depleted tropical oceanic waters generates a local winter bloom (Hu et al., 2004). Reverdin et al. (2021) estimated the freshwater lens to extend over $100,000$ km² and to a depth of ~ 40 m such that a few days later, the Chl-*a* imprint of the Amazon plume covered a large fraction of the study area (Figure 2f) and partially overlapped mesoscale eddies. This indicates that the structuring of the fronts is no longer driven by the ocean dynamics alone, but also by their interaction with the freshwater plume dynamics. Overall, the three snapshots of surface Chl-*a* in Figures 2d–2f show very different frontal patterns, indicative of the rapidly evolving dynamics, which, combined with their small spatial scales, suggest that their evolution falls in the domain of the submesoscale.

3.1.2. From In Situ Saildrones Observations

Despite a similar resolution as surface Chl-*a*, SST satellite maps do not reveal such structures (Figure 1c). Given the dispersion of the large freshwater plume, we expect these fronts to have a strong SSS signature. However the

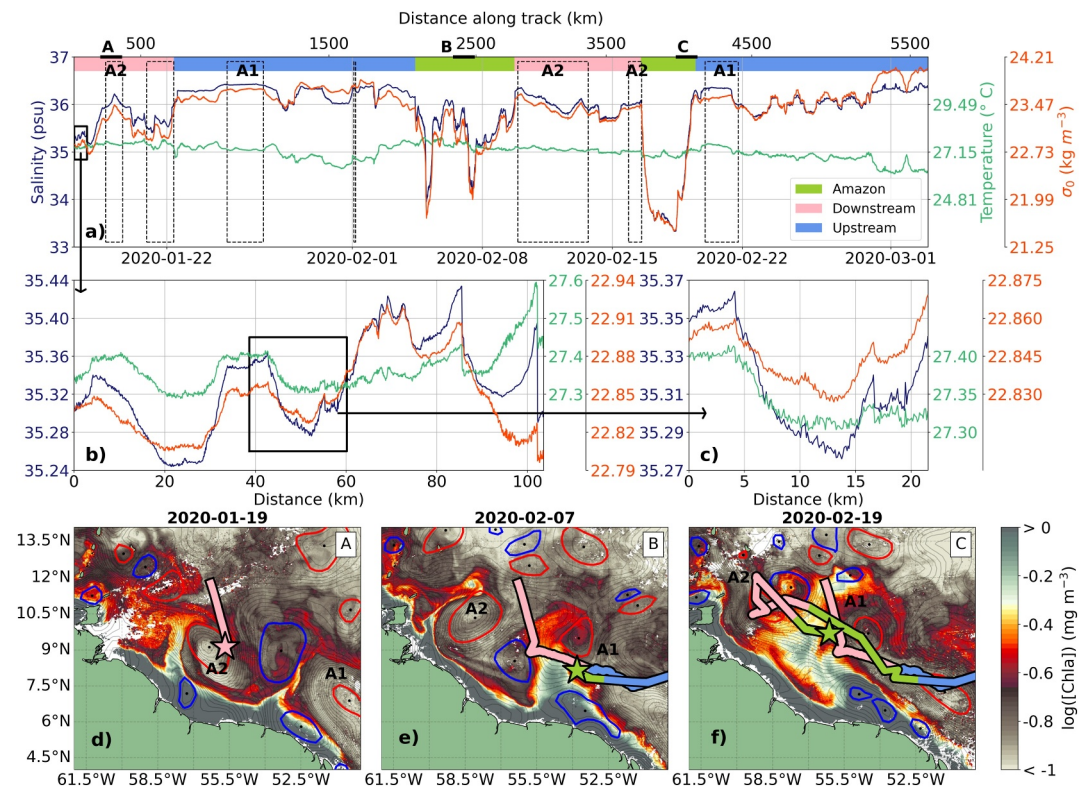


Figure 2. (a) Time series of surface salinity (blue), temperature (green) and potential density (orange) from 7 weeks of the SD1026 mission. Colored bars at the top indicate the different regions and dashed black contours indicate eddy crossings. An extended view of the time series as a function of distance is shown for (b) a 100- and (c) a 20-km section. In panels (a)–(c), T and S have been scaled proportionally—by the thermal expansion and haline contraction coefficients respectively α and β —so that equal displacements lead to equal effects on density. (d)–(f) Snapshots of surface Chl-*a* illustrating different ocean dynamical processes encountered during the SD1026 mission. They are labeled from A to C in (a). The trajectory of the SD1026 up to the time of the snapshot is shown by a line colored with the different regions with its last position indicated by a star. The NBC rings have been identified as A1 and A2 in (a) and (d)–(f).

SSS satellite product is too coarse to resolve the submesoscale fronts and freshwater filaments (Figure 1b). Even the salinity gradients associated with the plume contours are barely resolved and smoothed as a result of the satellite resolution. The Saïdrones observations provide a detailed and more clear picture of the surface fine-scale gradients, such as the three strong salinity dips measured by SD1026 as it navigated over the plume edges (Figure 2a). As a first-order estimate, salinities change by ~ 1.5 psu on the 5th, 1 psu on the 7th, and 2 psu on the 16th of February 2020 over ~ 15 , 10, and 40 km, respectively.

In Figures 2a–2c salinity (S) and temperature (T) have been scaled with the thermal expansion and haline contraction coefficients respectively, so that equal vertical displacements along the T and S axes lead to equal effects on density. As expected in a region near large river outflows, salinity variations control the horizontal density gradients, while temperature, which is nearly uniform along the Boulevard des Tourbillons (Figure 1b) plays a secondary role (Figure 2a). However, a closer look at sections of the time series (Figures 2b and 2c) reveals that T and S are more coherent on smaller length scales which couldn't be unveiled by satellite data. T and S are said to be partially compensated, resulting in reduced density gradients compared to their thermohaline counterparts (Figures 2b and 2c). This appears to hold throughout the entire survey. The detailed view of the upper ocean derived from the Saïdrones observations will be used to further investigate the relationship between salinity and temperature at varying length scales.

3.2. Submesoscale Compensation Developing Along Restratifying Fronts

3.2.1. Shear as a Proxy for Stratification

The Saildrones did not measure subsurface profiles of temperature and salinity but their ADCPs can be used to infer the upper ocean stratification. Foltz et al. (2020) observed that the vertical shear of the horizontal velocity

$$S^2 = (\partial_z u)^2 + (\partial_z v)^2$$

tends to be largest below the mixed layer. This may be the result of the propagation of internal waves under the mixed layer or the transfer of wind momentum or buoyancy forcing within the upper layer that generates enhanced shear.

Since no vertical sections of hydrographic properties were co-located with the Saildrones velocity measurements, the relationship between S^2 and the upper ocean stratification was investigated by comparing vertical hydrographic profiles acquired by the EUREC4A-OA/ATOMIC different observing platforms with any Saildrones ADCP profiles that met the criteria on space, time and T and S surface values. For each vertical profile collected during the experiment—by CTDs, underway CTDs (uCTD), moving vessel profilers (MVP), Argo floats and underwater gliders—we search for Saildrones observations within a 50-km radius at ± 1 day. Given the large fine-scale variability that can be found within the selected spatial area, criteria for T and S surface values are also applied. SST and SSS Saildrones observations must be $\pm 0.05^\circ\text{C}$ and ± 0.05 psu from the vertical profile upper values of T and S. For each selected Saildrones ADCP profile, the vertical shear is estimated and an average S^2 profile is calculated. The depth of the first local maximum exceeding $1 \times 10^{-4} \text{ s}^{-2}$ is taken as the MLD estimate, hereafter referred to as $\text{MLD}_{\text{shear}}$. The choice not to select the depth of the maximum shear was made because of the presence of a barrier layer associated with the freshwater plume. The strongest shear tends to be observed near the main thermocline in our data set, while a smaller peak can be found at the base of the freshwater upper layer. However, as we aim to detect a significant peak within the shear profile, a threshold is applied. Regarding the MLD derived from the associated vertical profile, a density threshold of 0.03 kg m^{-3} with a reference depth of 10 m (de Boyer Montégut et al., 2004) is applied.

These restrictive criteria resulted in only 54 vertical profiles being co-located with Saildrones ADCP observations. Two main patterns emerge from this co-location. A first pattern corresponds to when $\text{MLD}_{\text{shear}}$ and MLD coincide (Figure 3b, 29 profiles). The second pattern shows when the $\text{MLD}_{\text{shear}}$ is detected vertically in between the residual fresh upper layer and the main thermocline (Figure 3c, 19 profiles). The remaining profiles show a more complex relationship. As a result, we observe that $\text{MLD}_{\text{shear}}$ is deeper than MLD, with a greater spread observed for MLD shallower than ~ 40 m for which fresher profiles fall closer to the 1:1 line, while $\text{MLD}_{\text{shear}}$ is much higher than MLD for high SSS values (Figure 3a). This suggests that where the upper freshwater layer remains relatively fresh, there is a strong signature of the shear at the base of this layer. Where it becomes saltier, the peak of the shear that we detect is shifted toward the main thermocline (Figure 3c). We suggest that the change in the T-S properties of the fresh surface layer is the result of vertical mixing that brings up the saltier subsurface waters into the fresh water layer. Thus, the signature of the shear for the saltiest profiles within shallow MLD environment may more likely indicate a mixing layer depth, deeper than the MLD.

3.2.2. Restratifying Fronts: Case Studies

Considering that the Saildrones ADCP can provide a picture of the upper ocean stratification through the vertical shear S^2 , we observe that the submesoscale compensation which was already highlighted within the Saildrones T-S time series (Figures 2b and 2c) tends to occur at restratifying frontal regions. Three different sections have been selected to illustrate this observation (Figures 3d–3f). The crossing of a fresh surface layer is manifested as a strong shear signal appearing in the upper 30 m simultaneously as a drop in the surface salinity values. In Figures 3d and 3f, the restratification of the fresh surface layer is clearly visible in the shear, with a signal starting from the surface at the front and getting progressively deeper, highlighting the subsidence of the front. The signature of the main thermocline around ~ 60 m, identified before the crossing of the front, persists under the fresh layer, but with a slight increase toward shallower depths as the shear signal of the fresh layer deepens. On these three sections, a temperature gradient that partially compensates for the salinity front is observed just where

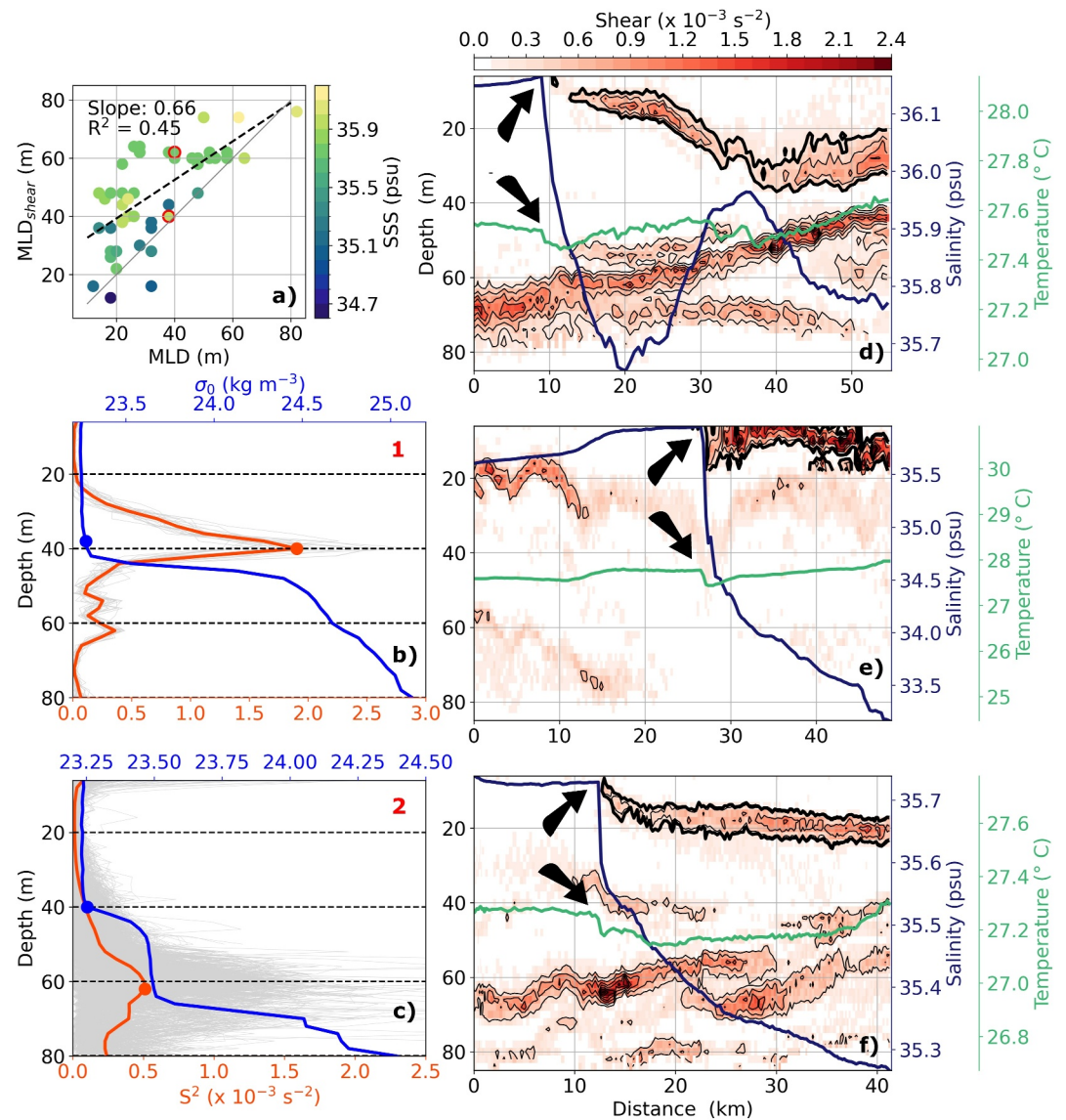


Figure 3. (a) MLD computed from vertical density profiles (blue line in (b)–(c)) as a function of MLD_{shear} estimated from shear profiles (red line in (b)–(c)) resulting from averaging over selected Sailldrones profiles (gray lines in (b)–(c)), given criteria on space, time, and T and S surface values. The black dashed line shows the best linear regression, while the thin gray line is the 1:1 line. (b)–(c) Two main patterns, representative of (b) 54% and (c) 35% of the profiles, showing how the distribution in (a) was obtained. The MLD and MLD_{shear} are shown as a blue and red dot, respectively. (d)–(f) Vertical shear sections (left axis) with temperature (green) and salinity (blue) time series superimposed from the Sailldrones observations. T and S have been scaled proportionally to highlight the partial temperature compensation of the salinity-dominated front, indicated by black arrows in each section. Iso-shear contours are shown in black with particular emphasis on the restratifying layer in the upper 30 m (bold contour).

a surface shear signal becomes apparent, suggesting that submesoscale compensation occurs at restratifying fronts.

Similar observations have been made in the Bay of Bengal, which is also under the influence of large freshwater inputs (Spiro Jaeger & Mahadevan, 2018), combining thermosalinograph and uCTD measurements. Using a process study model, they showed that enhanced surface cooling of the shallower and less saline surface mixed layer leads to increased T-S coherence at small scales. Because they are dynamically unstable, submesoscale fronts slump and they are characterized by very shallow stratification, making them the places where temperature compensation is expected to be reached first.

This mechanism relies on salinity-dominated gradients and a cooling flux. Spiro Jaeger and Mahadevan (2018) estimated the likelihood of both necessary factors to be met in the ocean from climatology data and found this cooling-induced compensation could be active in the northwestern tropical Atlantic during winter months. In what follows, the Saildrones observations are used to investigate the prevalence of scale-selective partially compensated fronts in the EUREC4A-OA/ATOMIC domain and to refine Spiro Jaeger and Mahadevan (2018) prediction.

3.2.3. Regional Approach

The presence of salinity-dominated gradients is expected to depend on both the freshwater plume dispersion pathway and the frontogenetic/frontolysis activity. In particular, intense mesoscale eddy processes sharpen fronts through stirring, while submesoscale instabilities cause fronts to collapse. As it can be seen in Figure 1d, the Saildrones sampled the northwestern tropical Atlantic extensively, from the Trade Wind Alley and the Boulevard des Tourbillons to the NBC retroflection. In addition to these already very different ocean dynamics, SSS satellite maps suggest that these environments are not similarly altered by the freshwater plume detachment. Given these differences, the EUREC4A-OA/ATOMIC domain was divided into four sub-regions.

The Tradewind region, where only SD1064 operated, is considered representative of the open ocean. Observations made outside of the warm eddy corridor, north of the dashed black line in Figure 1d, were selected to be representative of the Tradewind region. The other three sub-regions are all within the Boulevard des Tourbillons: near the freshwater plume is the Amazon region, while the areas north and south of it are referred to as the Downstream and Upstream regions, respectively. Dynamically, the Downstream region corresponds to the area where the plume is transported by currents and stirred by mesoscale eddies. The Upstream region is expected to be less influenced by this freshwater input. However, the presence of an NBC ring (A1) channeling the plume appears to generate a southeastward recirculation of some of the freshwater (Figures 2e and 2f). The subdivision of the Boulevard des Tourbillons area was made using both the Saildrones data and remotely sensed observations in order to follow the evolution of the different dynamical features in space and time.

The Saildrones started their journey off the south coast of Barbados within the Upstream region and traveled south toward the NBC retroflection. At this point, the plume had not detached yet from the coast. We consider the transition between the Upstream and Downstream regions to occur when the SSS exceeds 36 psu and the Saildrones are located east of 53°W. This corresponds to the crossing of the NBC retroflection front. Later on, in early February, the Saildrones navigated northwards toward the Upstream region. In doing so, they crossed a region strongly affected by the Amazon plume. We derive the position of the plume from satellite SSS maps. The transition between the Downstream and Amazon regions is identified when the SSS drops below 36 psu and the Saildrones are located west of 52.5°W. The next transition—between the Amazon and Downstream regions—is identified by a SSS exceeding 36 psu and the Saildrones located west of 56°W. Finally, the Saildrones traveled south, crossing the plume again before reaching the Downstream region. The section within the plume is well defined by the two large salinity fronts (Figure 2a), corresponding to the crossing of the plume's edges.

Due to its different sampling rate, the SD1064 time series was only used to describe the Tradewind sub-region. From this regional split, two sub-tracks are used for the Tradewind region compared to eight for the other regions. These sub-tracks are very heterogeneous in length, ranging from 305 km (Amazon) to 2,574 km (Tradewind).

3.3. Density Ratio Over Varying Horizontal Scales

The highlighted sections in Figures 3d–3f have been taken from both the Amazon and Downstream regions. In the following, we try to evaluate if this temperature and salinity coherence at small scales is a recurring pattern in the full Saildrones data set and in particular if it is observed in the Upstream and Tradewind regions as well. Assessing the prevalence of these structures is essential as the combination of T-S variations governs the resulting density gradients and frontal dynamics.

The density ratio R (Equation 1) was used to quantify T-S relation along the Saildrones tracks. To get an estimate of R over a wide range of scales, wavelet transforms of the T and S time series were performed to quantify the thermohaline fluctuations (ΔT and ΔS in Equation 1) as a function of spatial scale over different regions. The density ratio R was then estimated from these wavelet coefficients.

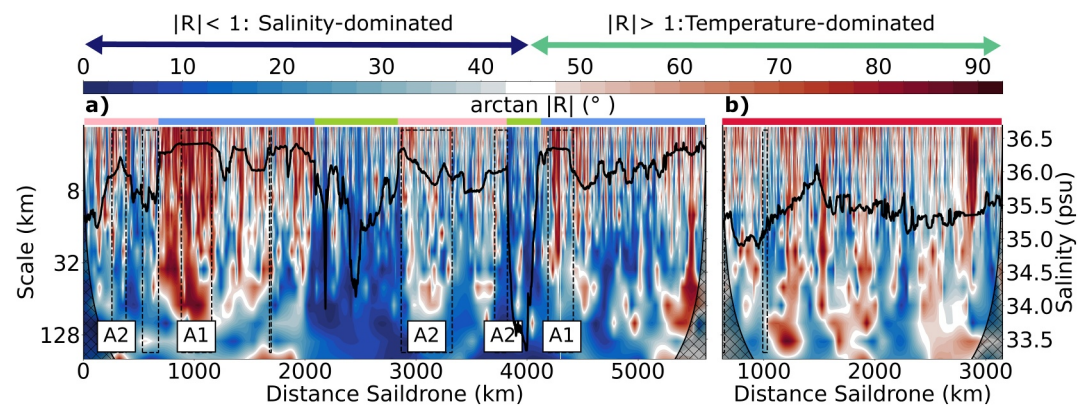


Figure 4. Norm of the density ratio, R , computed from the wavelet coefficients of the temperature and salinity time series of (a) SD1026 and a section of (b) SD1064 and plotted at scales from 2 to 200 km. The salinity time series is shown as a black line and eddy crossings are shown as black dashed lines. Data below the shaded area, known as the cone of influence, suffer from boundary effects and should be ignored. Colored bars at the top are a reminder of the different regions: Amazon (green), Downstream (pink), Tradewind (red), and Upstream (blue).

Figure 4 shows $\arctan |R|$ for scales from 2 to 200 km computed from SD1026 time series (Figure 4a) and a section of SD1064 (Figure 4b) plotted as a function of the distance traveled. At scales of $\mathcal{O}(100$ km), all over the Boulevard des Tourbillons (Figure 4a), salinity variations dominate ($|R| < 1$) due to the freshwater plume forcing. Further away from the coast, within the Tradewind Alley (Figure 4b), both salinity- and temperature-dominated fronts are found, but with $\arctan |R|$ being close to 45° , indicating that temperature and salinity gradients are of similar magnitude. Moving to smaller scales reveals much more variability associated with small and poorly correlated T and S gradients, resulting in a wide range of density ratios. In fact, in the absence of strong density gradients, mechanical stirring homogenizes T and S anomalies indiscriminately and does not select a particular density ratio. On fine scales, reduced horizontal salinity gradients also lead to poorly defined density ratios ($|R| \gg 1$) and thus to regions where temperature variations seem to largely dominate. Such regions can be observed at ~ 400 km, between 700 and 1,100 km and again at $\sim 4,200$ km of the SD1026 cruise (Figure 4a) and at 2,800 km for SD1064 (Figure 4b). This signal appears to extend from the smallest scale to scales comparable to the distance over which the salinity remains fairly constant, suggesting that this temperature-dominated signature is only the result of the salinity variations tending to zero. On the contrary, the strongest salinity gradients remain salinity-dominated, even at the smallest scales. This is particularly evident within the Amazon region where the strongest salinity drops are observed, but also locally across the other regions, such as around ~ 500 km for SD1026.

Strong differences in the magnitude of the density ratio and thus the contribution of the T and S gradients to the density fronts can be identified from these sections alone. The frontal gradients in the Amazon region are salinity-dominated at all scales. In the Upstream region, they are temperature-dominated at small scales due to weak horizontal salinity gradients and salinity-dominated at large scales, whereas in the Downstream region, especially between $\sim 3,000$ and 3,800 km of the SD1026 cruise (Figure 4a), $\arctan |R|$ takes values closer to 45° , particularly at small scales. This indicates that temperature and salinity gradients are of similar magnitude. Comparable observations are made in the Tradewind region but they hold at all scales (Figure 4b). The different regimes found in the Downstream and Upstream regions can be partly attributed to the interaction between the NBC rings crossed by SD1026 and the freshwater plume, which has affected their surface signature. A1, within the Upstream sector (Figure 4a at 1,000 and 4,300 km), has preserved a rather homogeneous SSS signature even after the plume detachment, inducing a biased temperature-dominated signal. On the contrary, the SSS of A2 has been eroded during the northwestward migration and shows a more complex SSS pattern consisting of horizontal salinity fronts (Figure 4a at 3,100 km).

To further explore the regional differences and assess T-S patterns at different length scales, the bivariate histograms of $\arctan |R|$ and ϕ for scales between 0.8 and 50 km were obtained for the four regions (Figure 5). They were determined by computing the wavelet coefficients of T and S for each subtrack of the Saildrones time series belonging to the same region. Then, after removing the points falling under the cone of influence, only the largest

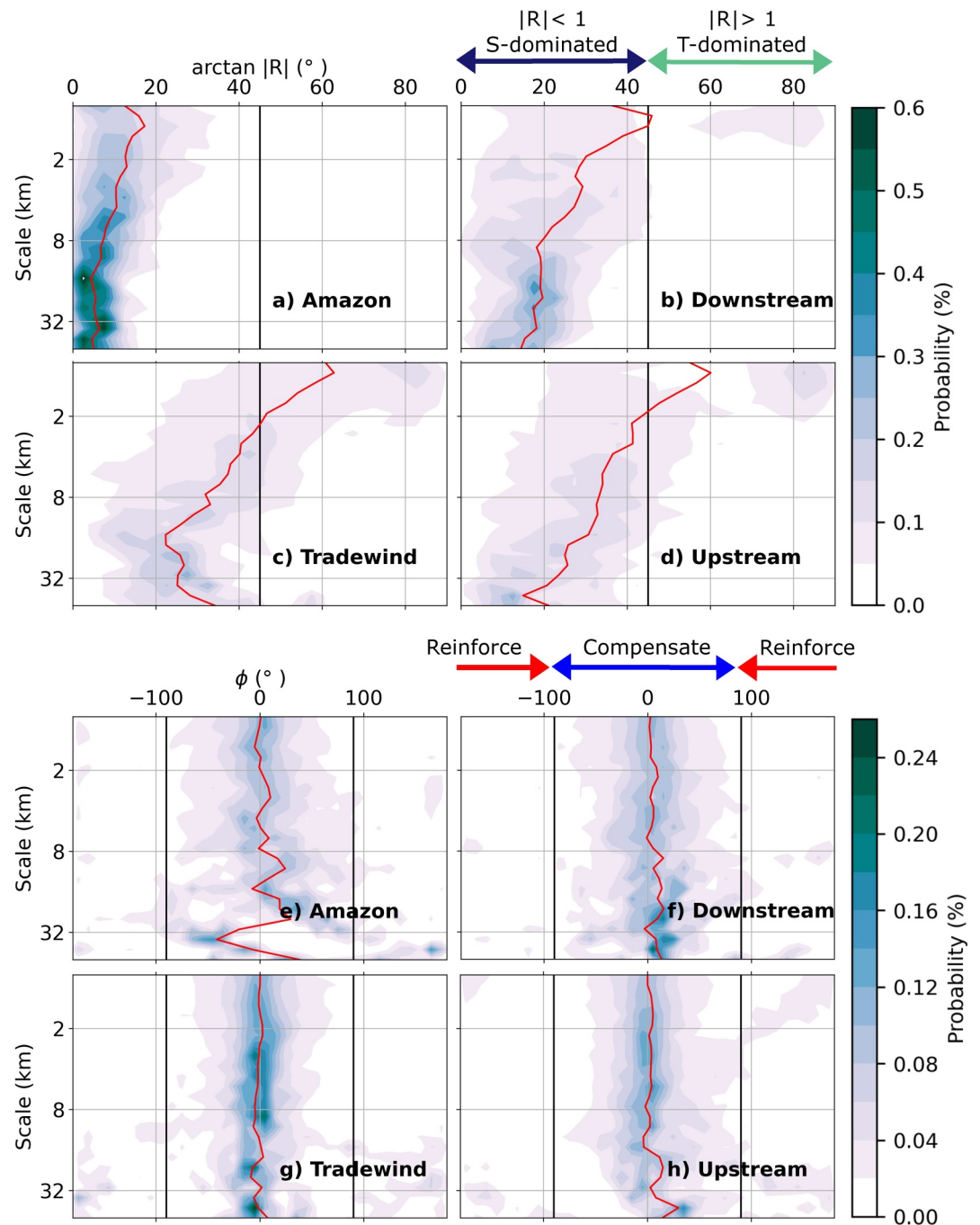


Figure 5. Bivariate histogram of (a)–(d) $\arctan |R|$ and (e)–(h) ϕ for length scales from 0.8 to 50 km computed from the 20% highest scaled coefficients ($\alpha\Delta T$, $\beta\Delta S$ in Equation 1) for each region at each scale. The red line corresponds to the median of the distributions at each scale. (a)–(d) The vertical black line at 45° indicates the transition between the salinity-dominated region and the temperature-dominated region. (e)–(h) The vertical black line at $\pm 90^\circ$ indicates the transition between the region where T and S compensate and the region where they intensify.

20% of these coefficients for each region at each scale are kept to compute R and derive the bivariate histograms. This is done to remove poorly defined density ratios associated with horizontal salinity gradients that tend to zero.

Figures 5e–5h show that T and S gradients are in phase ($\phi \sim 0$) in all regions at all length scales, implying that they act together to reduce the density magnitude of the fronts. However, for the Tradewind region, an increase in the

number of wavelet coefficients leading to $|\phi| > 90^\circ$ is observed at scales higher than ~ 8 km. This indicates that for some fronts, T and S are out of phase, leading to enhanced density variations.

Overall, the bivariate histograms of $\arctan |R|$ (Figures 5a–5d) are consistent with the first observations made from the time series (Figures 4a and 4b). The Amazon region stands out from the other regions with fronts strongly dominated by salinity (from $|R| = 0.1$ at 50 km to $|R| \sim 0.3$ at 1 km). The Downstream region, which receives freshwater from both the plume and coastal waters through eddy stirring, shows higher T-S compensation than within the Amazon region at all scales. In particular, between 8 and 50 km where the distribution remains relatively centered, $|R|$ is about 0.35. This suggests that as the freshwater anomaly is advected to the northwest, the salinity fronts are progressively compensated. Regarding the Tradewind region, the distribution of $\arctan |R|$ (Figure 5c) differs from the general pattern observed for the areas within the Boulevard des Tourbillons. There, the shift of the median toward larger values of $\arctan |R|$ at smaller scales is not linear. Fronts are more compensated at 50 km ($|R| = 0.7$) than at ~ 16 km, where the median of $\arctan |R|$ reaches its minimum ($|R| = 0.4$). This scale, where the salinity contribution is the strongest may be related to the size of the freshwater structures resulting from the stirring of the plume by the mesoscale motions that are advected toward the open ocean.

All the bivariate histograms reveal salinity-dominated fronts at large scales (~ 50 km) with an increasing contribution of T gradients with decreasing length scale, as indicated by the shift of the median toward larger values. This suggests the increased T-S coherence at small scales highlighted in the sections in Figures 3d–3f is a recurring pattern. However, for length scales smaller than ~ 2 km, the median falls into the temperature-dominated region for the Upstream and Tradewind regions. This shift is partly driven by a larger spread in the distribution along with a peak around 90° for the Downstream, Tradewind and Upstream regions (Figures 5b–5d). This points toward the issue of poorly defined density ratios due to disappearing salinity gradients, as previously mentioned. On the contrary, no peak around 90° is observed in the Amazon region where we can suspect stronger salinity gradients were measured.

Thermohaline surface gradients distributions will provide further insight to discard biased increased T-S coherence at small scales and to understand the difference in the compensation levels between the region.

3.4. Length Scales of Horizontal Surface Gradients

3.4.1. Fronts Magnitude

To depict the fronts quantitatively, the Saildrones temperature and salinity measurements are spatially subsampled on length scales ranging from 0.1 to 15 km to show multi-length histograms of surface thermohaline gradients (Figure 6a), as per Swart et al. (2020). All regions show a similar behavior of a sharp drop in surface thermohaline gradients with increasing sampling length scale. However, differences in the magnitude and decay rate of the sampled fronts are evident. Comparing the different regions and assessing the scale sensitivity of the fronts was achieved by fitting the 99-envelope of each distribution with an exponential decay function m of the form $m(x) = Ae^{-x/\lambda} + B$. $m(x)$ gives an indication on the strength of the highest gradients expected to be measured for a sampling scale x . The magnitude of the fronts was compared at two different scales: 0.1 and 10 km, respectively given by $m(0.1)$ and $m(10)$ and later referred to as $\nabla_{0.1}$ and ∇_{10} .

The magnitude of the salinity fronts shows strong regional variability, with the Amazon region containing the highest salinity gradients measured, being about three times larger in magnitude at all scales considered (Figure 6c). In this area, the freshwater anomaly is in its early stages, forming a rather coherent plume whose edges mark a sharp transition to the saline surrounding waters (Figures 1b and 2a). As the plume is advected northwestward, stirred by eddies, the fine-scale salinity fronts tend to be eroded by lateral mixing with the surrounding waters, significantly reducing the amplitude of salinity fronts observed in the other regions. However, smaller differences also appear between these three other regions with the strongest salinity gradients measured at fine scales (0.1 km), in both the Downstream and Tradewind sectors, both of which are downstream of the freshwater plume path. This is evidence of the influence of the freshwater plume far into the open ocean. At larger scales (10 km), stronger salinity gradients are instead observed in the Downstream and Upstream regions. This may indicate that the SSS field of the Tradewind area is rather homogeneous at the mesoscale, with fine-scale freshwater filaments resulting from the stirring of the plume by mesoscale motions. The slightly higher salinity gradients (Table 2) within the Boulevard des Tourbillons at 10 km could also result from the more intense mesoscale eddy activity. The regional differences in the amplitude of the temperature gradients are less

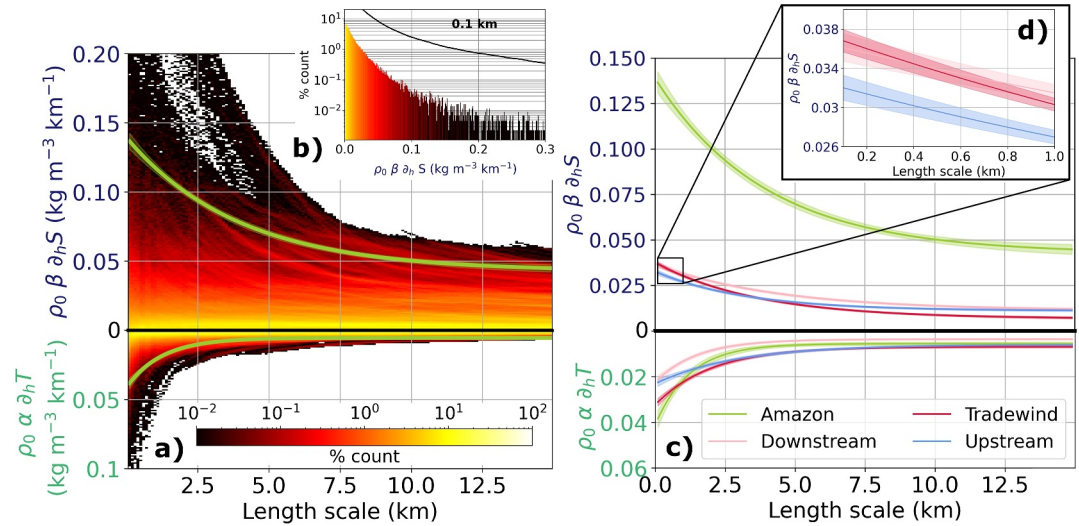


Figure 6. (a) Distribution of surface salinity (top) and temperature (bottom) gradients for horizontal length scales from 0.1 to 15 km. The logarithmic color scale shows the percentages at the different scales. Both $\partial_h S$ and $\partial_h T$ have been scaled to have density gradients unit ($\text{kg m}^{-3} \text{km}^{-1}$). The green lines are the exponential 99-envelope fits to the two distributions. (b) Distribution of surface salinity gradients for the smallest scale (0.1 km), with the black line indicating the cumulative histogram. (c) Exponential fits to the distributions of the surface salinity (top) and temperature (bottom) gradients for the four regions. The shaded envelope gives the confidence bands (3σ) from the uncertainties in the best-fit parameters. (d) Zoom of (c) for the salinity distribution at scales below 1 km.

pronounced. As expected from the SST satellite maps (Figure 1c), strong SST gradients are found within the Tradewind area. However, at smaller scales (0.1 km), SST gradients are the strongest within the Amazon region. This may result from the partial compensation at the submesoscale of the salinity-dominated fronts observed in Figure 5a.

A USV Sailbuoy survey in the Antarctic Marginal Ice Zone during the austral summer reveals surface density gradients reaching up to $0.06 \text{ kg m}^{-3} \text{ km}^{-1}$ for a sampling resolution of $\sim 0.5 \text{ km}$ (Swart et al., 2020). At the same spatial scale, the highest lateral density gradients measured by the SAILDRONES during the EUREC4A-OA/ATOMIC field experiment were found to be significantly stronger in all regions. They were only about two times larger in the Tradewind and Upstream regions, but up to five and 10 times larger in the Downstream and Amazon regions, respectively.

3.4.2. Compensation Timescale

From the derived T and S fronts at 0.1 and 10 km respectively ($\nabla_{0.1}$ and ∇_{10} in Table 2), the magnitude of two density ratios, $|R_{0.1}|$ and $|R_{10}|$, can be estimated (Table 3) following Equation 1:

$$|R_{0.1}| = \frac{\bar{\alpha} \nabla_{0.1} T}{\bar{\beta} \nabla_{0.1} S} \quad \text{and} \quad |R_{10}| = \frac{\bar{\alpha} \nabla_{10} T}{\bar{\beta} \nabla_{10} S}$$

with $\bar{\alpha}$ and $\bar{\beta}$ the average thermal expansion and haline contraction coefficients for each region. $|R_{0.1}|$ and $|R_{10}|$ should be considered with caution as they were calculated using the magnitude of the strongest T and S fronts (derived from fitting the 99th percentile envelope of each distribution), which are not necessarily co-located. However, consistent observations are found with the detailed study of T-S coherence using the wavelet analysis (Section 3.3). The three regions within the Boulevard des Tourbillons show similar behavior with salinity-dominated fronts with increasing temperature contribution moving to smaller scales. The reduced magnitude of the density fronts at 0.1 km compared to the salinity contribution to the fronts suggests

Table 2

Magnitude of the Fronts at 0.1 and 10 km, $\nabla_{0.1}$ and ∇_{10} ($\text{kg m}^{-3} \text{km}^{-1}$) Respectively, Resulting From Fitting the 99-Envelope of Multi-Length Histograms of Salinity, Temperature and Density Surface Gradients for Each Region

| Regions | | Salinity | Temperature | Density |
|------------|----------------|----------|-------------|---------|
| Amazon | $\nabla_{0.1}$ | 0.137 | 0.038 | 0.135 |
| | ∇_{10} | 0.050 | 0.006 | 0.047 |
| Downstream | $\nabla_{0.1}$ | 0.036 | 0.021 | 0.030 |
| | ∇_{10} | 0.014 | 0.004 | 0.014 |
| Tradewind | $\nabla_{0.1}$ | 0.037 | 0.031 | 0.033 |
| | ∇_{10} | 0.009 | 0.007 | 0.013 |
| Upstream | $\nabla_{0.1}$ | 0.032 | 0.022 | 0.028 |
| | ∇_{10} | 0.012 | 0.007 | 0.011 |

Table 3

Density Ratios $|R_{0.1}|$ and $|R_{10}|$ Computed From the Magnitude of the Temperature and Salinity Fronts Sampled at 0.1 and 10 km (Table 2) Derived by Fitting the 99th Percentile Envelope of Multi-Length Histograms for Each Region

| | Amazon | Downstream | Tradewind | Upstream |
|-------------|--------|------------|-----------|----------|
| $ R_{0.1} $ | 0.28 | 0.59 | 0.84 | 0.70 |
| $ R_{10} $ | 0.11 | 0.26 | 0.81 | 0.54 |

that T and S are in phase and thus partially compensate (Table 2). For the Tradewind region, the fronts at 0.1 km are still salinity-dominated ($|R_{0.1}| < 1$), further indicating the presence of freshwater filaments well into the open ocean. At 10 km, however, the magnitude of the density fronts is larger than both the salinity and temperature fronts (Table 2), suggesting that T and S are out of phase and amplifying the density variations.

Furthermore, as already observed from the wavelet analysis, the stage of compensation is higher in all of the regions compare to the Amazon, all scales considered (Figures 5a–5d, Table 3). Considering that the mechanism

described by Spiro Jaeger and Mahadevan (2018) is at play to explain the partial compensation of the salinity-dominated fronts, it is straightforward that the required temperature change to achieve full compensation is smaller and is thus achieved faster the weaker the magnitude of the salinity front (ΔS in Equation 2), assuming an equivalent heat flux cooling forcing.

Considering an initially strongly salinity-dominated front, it is possible to get an estimate of the compensation rate by computing the temperature change δT over a time Δt of both the fresh and the salty side of the fronts for a given net heat flux $Q_{net}(t)$:

$$\delta T = \frac{\int_{\Delta T} Q_{net}(t) dt}{\rho_0 c_p H}$$

with ρ_0 the mean density of seawater, c_p the specific heat capacity and H the MLD. This results in a change of the density ratio which can be expressed as:

$$\delta R = \frac{\alpha(\delta T_s - \delta T_f)}{\beta \Delta S} = \frac{\alpha}{\beta \Delta S} \frac{\int_{\Delta T} Q_{net}(t) dt}{\rho_0 c_p} \left(\frac{1}{H_s} - \frac{1}{H_f} \right) \quad (2)$$

where the subscripts s and f refer to the salty and fresh side of the front, respectively.

The net surface heat flux Q_{net} was estimated using ERA5 reanalysis data co-located with the Saildrones transect previously interpolated on an hourly basis. Daily mean heat flux of -40 , -32 , -26 , and -6 W m $^{-2}$ over the Amazon, Downstream, Tradewind and Upstream regions respectively were obtained. Despite daily mean Q_{net} not being strongly negative, in particular within the Upstream area, intense cooling occurs during nighttime where the net heat flux drops below -200 W m $^{-2}$ in all regions.

δR was estimated from Equation 2 considering an initially uncompensated ($R = 0$) 2.5-psu salinity front representative of the freshwater plume edges (Figure 2a). A net heat flux $Q_{net}(t)$ corresponding to the mean daily profile derived from ERA5 reanalysis data collocated with the Saildrones trajectory over the Amazon region was applied. From the analysis of the vertical profiles, a MLD of 15 and 40 m was chosen for H_f and H_s , respectively. Under these conditions, R has increased only by 0.6° , which corresponds to a compensation of 1% over one day. Assuming that ΔS and both H_f and H_s do not vary in time, arctan $|R|$ reaches $\sim 7^\circ$ after 20 days: the front is still strongly salinity-dominated ($\sim 16\%$ compensated). However, for a weaker 0.5-psu salinity front, the resulting density front is divided by 2 after 15 days.

This computation provides a conservative estimate of the compensation timescale as all of the parameters in Equation 2 are kept constant while a temperature front develops. It also does not take into account any short events of intense cooling which may accelerate the formation of the temperature front. However, given their relatively similar daily mean Q_{net} , it suggests that the higher degree of frontal compensation observed in the Downstream region compared to the Amazon (Figures 5a and 5b, Table 3) results from the weaker salinity fronts found in this area (Figure 6c, Table 2), for which the compensation is reached much faster.

The variability in the magnitude of the salinity-dominated fronts between the different regions is driven by the interaction between the ocean and the freshwater plume dynamics. The stirring of this freshwater lens by mesoscale eddying processes will sharpen the fronts until submesoscale instabilities can develop and cause the

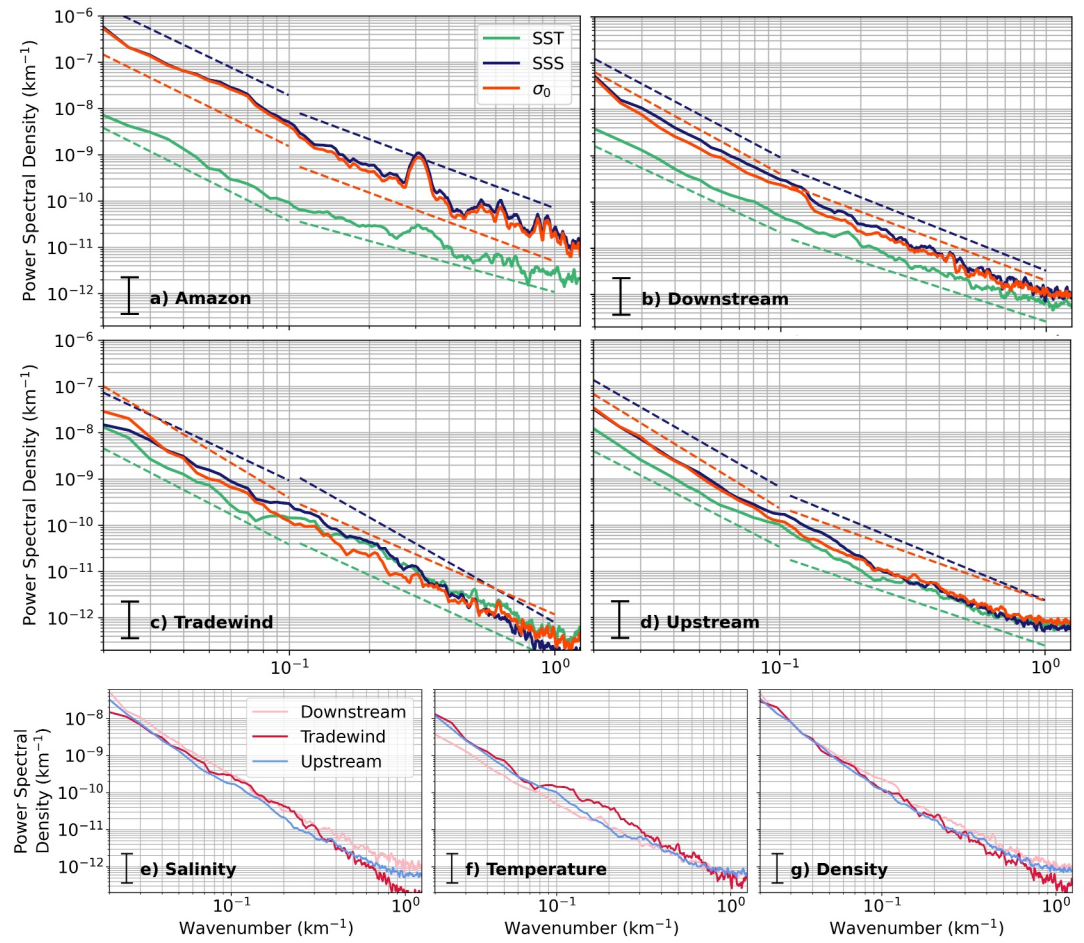


Figure 7. (a)–(d): Salinity (blue), temperature (green) and density (orange) power spectral density (PSD) for each region ((a): Amazon, (b): Downstream, (c): Tradewind, (d): Upstream) for length scales ranging from 0.8 to 50 km. Linear regression lines from 1–10 km and 10–50 km are shown as dashed line colored by the state variables they referred to. (e)–(g): (e) Salinity, (f) temperature and (g) density PSD for the Downstream (pink), Tradewind (red), and Upstream (blue) regions. To allow comparison between the PSD, they have been normalized in all panels by β^2 , α^2 and $1/\rho_0^2$, for salinity, temperature and density respectively. The 95% confidence interval computed from a chi-square approach is shown.

fronts to slump. Power spectral density estimates were investigated to compare the strength of these processes in the different regions.

3.5. Thermohaline Spectra

Remote and in situ data have revealed a region rich in mesoscale eddies and filaments over a wide range of length scales, from $\mathcal{O}(0.1)$ km to $\mathcal{O}(100)$ km. To investigate the dynamics which may explain this observed thermohaline horizontal variability, power spectral density (PSD) estimates of surface salinity, temperature and density were computed over wavelengths of 0.8–50 km. For each region, the sub-tracks are first linearly interpolated to 0.4 km, the coarser spatial resolution of the Saildrones data set (Table 1), and then divided into 200 km non-overlapping equal segments. For each transect, the mean is removed before the spectrum is estimated using the multitaper method (Prieto, 2022). The PSD on Figures 7a–7g result from the averaging of all segments spectra for each region. Two best-fit wavenumber slopes are retrieved from these PSD: k_{1-10} and k_{10-50} , computed over 1–10 km and 10–50 km respectively. To compare the PSD of density, salinity and temperature, they have been normalized by $1/\rho_0^2$, β^2 and α^2 respectively.

From the surface density spectra in Figure 7 we observe strong regional differences in the variance, with the Amazon being about 10 times more energetic than the other sectors all scales considered. Assuming that these

Table 4
Best-Fit Wavenumber Slopes, k_{1-10} and k_{10-50} , Estimated From Linear Regression of the PSD for the Different State Variables Over 1–10 km and 10–50 km Respectively, for the Different Regions

| Regions | | Salinity | Temperature | Density |
|------------|-------------|----------------|----------------|----------------|
| Amazon | k_{10-50} | -2.7 ± 0.4 | -2.9 ± 0.5 | -2.8 ± 0.4 |
| | k_{1-10} | -2.1 ± 0.4 | -1.6 ± 0.3 | -2.1 ± 0.3 |
| Downstream | k_{10-50} | -3.0 ± 0.6 | -2.7 ± 0.5 | -3.1 ± 0.6 |
| | k_{1-10} | -2.3 ± 0.5 | -1.9 ± 0.3 | -2.1 ± 0.4 |
| Tradewind | k_{10-50} | -2.7 ± 0.7 | -3.0 ± 0.6 | -3.5 ± 0.7 |
| | k_{1-10} | -3.3 ± 0.4 | -2.6 ± 0.5 | -2.5 ± 0.4 |
| Upstream | k_{10-50} | -3.3 ± 0.9 | -3.0 ± 0.8 | -3.5 ± 0.9 |
| | k_{1-10} | -2.4 ± 0.7 | -1.9 ± 0.5 | -2.0 ± 0.5 |

density spectra are a proxy for the potential energy spectra, it confirms that available potential energy (integration under the spectra, assuming N^2 to be constant) in the vicinity of the freshwater plume is much higher than in the other regions. It also suggests that as the freshwater lens is being stirred by the mesoscale eddy field, potential energy is converted into kinetic energy, the two main processes at play in the upper ocean being interior-baroclinic instabilities at the mesoscale and mixed layer instabilities (MLIs) at the submesoscale.

Despite large variability between the transects, the best-fit wavenumber slopes for the surface density PSD reveal a break from the mesoscale (10–50 km) to the submesoscale (1–10 km) with $k_{10-50} \sim -3$ and $k_{1-10} \sim -2$ for all regions within the Boulevard des Tourbillons (Figures 7a–7d and Table 4). This flattening of the spectral slopes could arise from different dynamics. In surface quasi-geostrophic theory, buoyancy gradients pass through stirring by geostrophically balanced flows resulting in strong submesoscale fronts at the

ocean surface which can lead in slopes ranging from $-5/3$ and -2 (Blumen, 1978; Lapeyre, 2017). Figure 6 and Table 2 revealed strong frontal structures, in particular within the Amazon region, suggesting fronts could be the cause of the ~ -2 spectral scaling at the submesoscale. A spectral slope close to -2 can also result from mixed layer dynamics with eddies confined within the mixed layer (Callies & Ferrari, 2013). These mixed layer eddies grow from MLIs which develop at the internal Rossby radius. MLIs convert available potential energy from mesoscale buoyancy gradients and energize submesoscale flows in the mixed layer. The internal Rossby radii ($L_r = NH/f$ where N is the mean buoyancy frequency computed over 2 m on both sides of the mixed layer mid-depth, H is the MLD derived from the density criteria and f is the Coriolis frequency) were estimated for this campaign by selecting the collected vertical profiles within the different regions. They were found to be 5.1 ± 2.2 km, 5.7 ± 3.6 km, 3.3 ± 1.2 km, and 7.4 ± 4.2 km for the Amazon, Downstream, Tradewind and Upstream regions respectively. So with internal Rossby radii of the order of $\mathcal{O}(1-10)$ km, we would expect mixed layer dynamics to be enhanced below 10 km (Boccaletti et al., 2007; Capet et al., 2008). However, MLIs tends to be damped out in shallow mixed layer environment which suggests that MLIs may not be so active in the Amazon region as in the other ones. At scales below the internal Rossby radius, we could also expect the ageostrophic component of the flow to become predominant. The break in the spectral slopes could then be explained by the shift from interior quasigeostrophic turbulence with $k \sim -3$ (Charney, 1971) to ageostrophic frontogenesis which sharpens gradients into fronts and flattens the spectral slope to $k \sim -2$ (Klein et al., 1998).

Normalization of the spectra allows the comparison of the different tracers with the density spectrum, which is used as a proxy for potential energy. We see a strong disparity in energy levels for the regions within the Boulevard des Tourbillons, especially at large scales (Figures 7a, 7b, and 7d). Temperature variations are less energetic than salinity variations, which account for most of the density fluctuations at all wavelengths, given their nearly identical spectra. This is consistent with the distribution of the surface thermohaline gradients, which revealed salinity-dominated fronts (Figure 6), and highlights all the energy that can be held within these salinity gradients. Note that the observed difference in energy levels between temperature and salinity reflects their relative contribution to density variations. It can thus be related to the previous density ratio estimates (Table 3), with which they are in good agreement, the largest energy disparity between T and S spectra being associated with the smallest density ratio magnitude (for a given length scale) and vice versa. The Tradewind region shows a different picture with the density spectrum being stronger than both T and S spectra (Figure 7c) at scales higher than ~ 30 km. This suggests that salinity and temperature variations act together to enhance density fronts at large scales which is once again consistent with the previous analysis.

Overall, the magnitude of the three state variables spectra remain similar for the Downstream, Tradewind and Upstream region with the exception of salinity (and density to a lesser extent) at the smallest scales (Figures 7e and 7g). The flattening of the wavenumber slopes at the submesoscale is not observed for the salinity spectra within the Tradewind region and is also not so pronounced for the density spectra (Table 4). This suggest the dynamics between the Boulevard des Tourbillons and the open ocean is quite different, with reduced submesoscale activity within the Tradewind Alley. It may be related to a less intense mesoscale eddy field.

For the regions within the Boulevard des Tourbillons, the energy difference between T and S spectra gradually decreases as we move to small scales. This is associated with significantly different spectral slopes, in particular at the submesoscale with $k_{1-10} \sim -2.2$ for salinity and a flatter slope for temperature ($k_{1-10} \sim -1.8$) (Table 4). This provides further evidence for partial compensation at small scales with increasing T contribution to the salinity-dominated fronts. If these tracer slopes remain consistent with submesoscale dynamics, both frontogenesis and mixed layer dynamics, resulting in slopes close to -2 , the difference between the two tracers may be due to their tracer-like behavior. In salinity-dominated regions, we could expect temperature to be a passive tracer and salinity to be an active tracer.

4. Discussion

This study investigates the fate of strongly salinity-driven fronts, formed by the recent detachment of a large freshwater plume, and as the plume is stirred and advected by mesoscale motions. Regional contrasts in surface thermohaline properties and their relationship have been revealed with a high-resolution data set.

4.1. Submesoscale Processes

Despite typically low river discharge in winter and a plume extension reaching its minimum (Fournier et al., 2017), off-shelf freshwater transport resulting from a change in wind direction and sustained by eddies stirring (Reverdin et al., 2021) led to the development of surface freshwater layers. At the surface, the advection of this low saline water resulted in mesoscale and sub-mesoscale horizontal salinity-dominated density gradients that have been observed at scales down to $\mathcal{O}(0.1 \text{ km})$. These salinity-driven lateral gradients, the largest of which are found in the vicinity of the Amazon plume, are strained and stirred by mesoscale eddies, leading to their intensification and promoting frontogenesis (McWilliams et al., 2009).

As these fine-scale freshwater filaments develop in response to the increased strain rate, an ageostrophic circulation is established with an upwelling on the fresh side of the fronts and a downwelling on the saline side (Klein & Lapeyre, 2009). Submesoscale mixed layer instabilities (MLIs) can also arise and the associated large vertical velocities lead to the exchange of water masses and energy through the base of the ML (Boccaletti et al., 2007). Recent numerical simulations and observations suggest that mesoscale baroclinic eddies are also unstable to different submesoscale instabilities leading to restratification and submesoscale subduction of water masses (Brannigan et al., 2017).

We cannot directly infer the effect of these submesoscale processes on the ML structure with our data set, but the observed flattening of the surface density spectral slopes from ~ -3 at the mesoscale (10–50 km) to ~ -2 at the submesoscale (1–10 km) (Figures 7a–7d and Table 4) suggests that they are active. A first explanation for these observations is that large-scale fronts resulting from the stirring of the freshwater plume by the mesoscale dynamics fuel mixed layer instabilities (MLIs), from which mixed layer eddies grow and form submesoscale fronts through stirring. However, the vertical stratification within the Amazon region may not allow MLIs to develop due to the presence of very shallow mixed layers. We could then argue that the spectral slope close to -2 in this region at the submesoscale results from the stirring of buoyancy gradients by geostrophically balanced flows (Blumen, 1978; Giddy et al., 2021; Lapeyre, 2017)—in our case, the NBC rings, and the NBC retroreflection. This is supported by the presence of strong frontal structures in the Amazon region (Figure 6, Table 2). As we move away from the freshwater anomaly in the Amazon region, the observed mixed layers tend to be deeper and the available potential energy, given by the integration of the density spectra assuming N^2 to be a constant, decreases (Figure 7). The drastically reduced magnitude of the density spectra could be interpreted as a result of the MLIs converting the available potential energy into kinetic energy. It is also consistent with the reduced strength of the submesoscale fronts (Figure 6c), which could indicate that they have slumped due to growing mixed layer eddies. However, compared to the Downstream and Upstream regions, the Tradewind region shows a steeper spectral slope at the submesoscale. This suggests that a different dynamic than MLIs may be at play outside of the Boulevard des Tourbillons.

The current data set does not allow to discriminate between the different mechanisms which may lead to a flattening of the spectral slopes at the submesoscale. Moreover, the steeper slopes found at the submesoscale for the density spectra compared to the -2 slope predicted by the different theories exposed above could indicate that multiple processes of submesoscale variability are active in these regions. Alternatively, it may arise from variability within individual transects of each region as well as from uncertainties in the spectral computation. In

addition, the data set contains only lower bound estimates of the slopes since it is more likely that the Saildrones did not cross the fronts perpendicularly. Due to their sampling resolution (Table 1), the detection of fine-scale features is also limited. These two biases would artificially steepen the spectral slopes equally in all regions.

4.2. Reduced Stratification From Cooling-Induced Submesoscale Horizontal Compensation

The data set shows increased horizontal compensation along restratifying submesoscale fronts, suggested to be due to a cooling heat flux. The modification of SST fronts by MLD horizontal variations due to a surface heat flux that modifies the mixed layer temperature inversely proportional to its depth has been observed at the mesoscale in other frontal regions such as the Agulhas Return Current region (Tozuka & Cronin, 2014) or the upstream Kuroshio Extension (Tozuka et al., 2017). It highlights how air-sea heat flux can counteract frontogenesis or frontolysis mechanisms associated with oceanic processes. The analysis of thermohaline fronts in the Bay of Bengal (Spiro Jaeger & Mahadevan, 2018), supported by similar observations we collected in the northwestern tropical Atlantic, suggests such mechanisms also occur at the submesoscale. This highlights the importance of reproducing the horizontal variability of the ocean mixed layer at small scales in coupled general circulation models, in order to correctly represent frontal air-sea interactions and their impact onto the ocean.

How this increased horizontal compensation at the submesoscale affects the stratification in our data set remains uncertain. As a horizontal temperature gradient is formed due to enhanced cooling over the shallower and fresher side of the front, the density difference between a fresh but slightly colder and a salty but slightly warmer water mass is reduced. As a result, we can expect along-isopycnal subduction of water at the front, leading to enhanced isopycnal T-S variance which can be stirred along isopycnals. Cross-isopycnal mixing would then bring saltier waters into the fresher waters and conversely, reducing the sharpness of the salinity front, but also the vertical stratification, in particular on the fresh side of the front which may lead to a deepening of the MLD. If the horizontal salinity front is partially compensated, the vertical salinity stratification is also partially compensated. In fact, cooling heat fluxes over freshwater layers can result in temperature inversions, which have been observed at some locations in the collected vertical profiles. It increases the value of the vertical density ratio toward 1 and thus reduces the vertical stratification, making it more likely to be destroyed by strong wind events. In any case if R_v exceeds 1, convective mixing will deepen the fresh layer MLD and mix the fresh water with the saltier deeper layers. This would also induce a decrease in the salinity front along with a vertical redistribution of the previously capped heat content. This could lead to a decrease in R as a result of a reduced horizontal temperature gradient. Overall compensation and weakening of the salinity fronts can be expected to be reached on a shorter timescale than what was estimated from Equation 2 considering all the parameters are kept constant.

This study assumes that surface horizontal thermohaline gradients arise essentially due to spatial and not temporal variations. However, it is not possible to distinguish between the temporal and spatial components of the gradients along the tracks. The extent to which the temporal evolution of the fronts may affect our results, in particular the magnitude of the fronts and the degree of compensation, cannot be determined. Figures 3d–3f reveals that compensation occurs on scales <1 km. Given the minimum speed of the Saildrones (Table 1), this corresponds to a time less than 20 min for observations taken across the fronts. Events of intense cooling, such as storms, can cross the fronts on such short time scales. Regarding compensation and considering an initially uncompensated front ($R = 0$, $\Delta T = 0$), it can induce higher values of R , with T and S compensating (reinforcing) when the Saildrones cross the front from the saltier (fresher) side. Intense winds could also dampen the strength of submesoscale fronts by increasing vertical mixing, in particular the salinity component due to the large difference in S between the fresh upper layer and the saltier waters below, leading to a more complex effect on R . However, from a statistical point of view, it seems reasonable to neglect the temporal component at these scales.

4.3. Implications

It remains difficult to attribute the evolution of the stratification to a single mechanism, as several competing processes can be at play. Here, we describe how submesoscale processes such as cooling-induced horizontal compensation or MLIs could actively modify the upper ocean stratification, eventually leading to significant vertical fluxes that erode the base of the ML. As the upper fresh layer mixes with the underlying warmer and saltier waters, the previously trapped heat would be released to the air-sea interface. These mechanisms would then potentially be critical in modulating ocean-atmosphere interactions.

The contribution of these fine-scale structures to air-sea fluxes has been highlighted by recent studies in the same geographical area. Fernández et al. (2023) show that fine-scale SST features significantly enhance latent heat flux due to the induced changes in the vertical stratification of the marine atmospheric boundary layer. Olivier et al. (2022) highlight the variability in air-sea CO₂ fluxes that occurs at both large and small scales, with salinity being one of the most valuable indicators of $f\text{CO}_2$ within the eddy corridor. However, assessing and predicting air-sea fluxes variations induced by the salinity field remain difficult due to the scarcity of in situ data and the coarse resolution of satellite salinity compared to temperature and chlorophyll. Overall, these studies have been limited by the lack of colocalized data of the upper ocean thermohaline structure along with the vertical stratification of the lower atmosphere.

However, assessing the contribution of submesoscale processes to ML changes or air-sea fluxes would remain challenging due to their short timescales, even with a complete picture of the vertical structure of the air-sea interface, including both the ocean mixed layer and the marine atmospheric layer (Swart et al., 2023). Monteiro et al. (2015) take advantage of the ability of USVs to operate over long periods of time, combined with their high temporal resolution, to show that a sampling resolution of less than 2 days is required in 30%–40% of the Southern Ocean to achieve the necessary accuracy in CO₂ flux estimates to reveal climate trends.

Over a day, the increase in the density ratio is hindered by the diurnal variations of Q_{net} : the cooling flux is limited to the nighttime, and we expect that the newly created horizontal temperature gradient is partially destroyed during the day, when a large heating flux warms the upper ocean. Hence we may observe stronger submesoscale density fronts during daytime compared to nighttime when thermohaline compensation is meant to be active. On a seasonal timescale, we expect that this increased submesoscale compensation will not be found in summer, when the net heat flux is positive (Bigorre & Plueddemann, 2021). On the contrary, it may lead to a strengthening of the salinity-dominated fronts and given that the Amazon River discharge progressively increases from March to May (Lentz & Limeburner, 1995), a more intense submesoscale activity is expected with stronger submesoscale density fronts as well.

High-resolution regional models could be used to overcome the limited temporal coverage of our data set and to further investigate the seasonality of the submesoscale activity. Fox-Kemper et al. (2008) proposed a parameterization for MLIs, in particular for the potential energy release, which has been verified in realistic model configurations (Capet et al., 2008; Mensa et al., 2013). However, this scaling assumes that the potential energy conversion is related to the buoyancy gradients, which are sharpened by the mesoscale strain field when the mixed layer is deep. Luo et al. (2016) investigated submesoscale processes in the northern Gulf of Mexico, a region under the influence of freshwater inflow from the Mississippi River system, using a regional model with submesoscale-permitting horizontal resolution. They show that this scaling fails to reproduce the potential energy release because the seasonal cycle of the freshwater flux—which drives the lateral density gradients—is out of phase with the seasonal variation of the mixed layer. This highlights the key role of the freshwater river input in the submesoscale activity. In the tropical Atlantic Ocean, the seasonal cycle of the MLD is weak (Foltz et al., 2003), while the Amazon River discharge shows strong seasonal variations (Lentz & Limeburner, 1995). This suggests that the Fox-Kemper et al. (2008) parameterization may not be appropriate for our region as well and highlights the need to develop new parameterizations. On the one hand, high-resolution regional climate models could facilitate the progress of improved parameterizations (Hewitt et al., 2022); on the other hand, the data set analyzed here could be used as a testbed for their development. We also show that the contribution of a freshwater forcing to frontogenetic processes can be critical, highlighting the need for reliable satellite salinity data, especially in coastal areas subject to riverine inputs. This result cannot be achieved without more extensive salinity in situ measurements in the same areas.

5. Conclusion

This study investigates the surface horizontal thermohaline gradients in the northwestern tropical Atlantic, where surface density gradients result not only from the mesoscale motions and atmospheric forcing, but also from the dynamics of the freshwater fluxes associated with the Amazon River system. Thus, the strongest gradients are found in the vicinity of the northwestward spreading freshwater plume. The attenuation of surface density gradients away from the plume suggests that freshwater fluxes are a first-order parameter driving frontogenesis. Mesoscale motions, in particular two observed NBC rings, stirred this freshwater anomaly offshore. Our results

suggest that this stirring of gradients enhances the horizontal strain and sets the conditions for submesoscale fronts to form through frontogenesis, and from which mixed layer eddies can grow.

While the large-scale fronts are strongly salinity-dominated, these submesoscale fronts are found to be partially temperature-compensated. The analysis of the Saildrones ADCP shear observations suggests that this compensation occurs at restratifying frontal regions. Because submesoscale fronts are dynamically unstable, they slump, leading to increased stratification along the front. The atmospheric cooling over the region during winter is expected to form a temperature gradient as a result of a larger SST response over the shallow mixed layer. The weakening of the submesoscale fronts due to partial temperature compensation prevents the cascade of energy to smaller scales where dissipation occurs. Overall, the applied methodology could be extended to other data sets to assess the phenomenology of fine-scale structures in other dynamical regions.

Data Availability Statement

This study makes use of numerous data sets made freely available and listed here.

- All the in situ observations collected during the EUREC4A-OA/ATOMIC experiment and used in this study (Saildrones, CTDs, uCTDs, Gliders, MVP, Argo floats, and Underwater Gliders) (Bony & Bjorn, 2021): <https://observations.ipsl.fr/aeris/eurec4a/#/>.
- SMAP maps produced by Remote Sensing System (RSS v4 70 km) (Boutin et al., 2021): <https://doi.org/10.5285/5920a2c77e3c45339477acd31ce62c3c>.
- Chl-*a* and SST maps produced by CLS (Olivier et al., 2022; Reverdin et al., 2021): <https://observations.ipsl.fr/aeris/eurec4a-data/SATELLITES/CLS/>.
- Global Ocean Gridded L 4 Sea Surface Heights And Derived Variables Reprocessed 1993 Ongoing (CLS, 2018): <https://doi.org/10.48670/moi-00148>.
- ERA5 (Hersbach et al., 2021): <https://doi.org/10.24381/cds.adbb2d47>.

References

- Androulidakis, Y., Kourafalou, V., Halliwell, G., Le Hénaff, M., Kang, H., Mehari, M., & Atlas, R. (2016). Hurricane interaction with the upper ocean in the Amazon-Orinoco plume region. *Ocean Dynamics*, 66(12), 1559–1588. <https://doi.org/10.1007/s10236-016-0997-0>
- Biddle, L., & Swart, S. (2020). The observed seasonal cycle of submesoscale processes in the Antarctic marginal ice zone. *Journal of Geophysical Research: Oceans*, 125(6), e2019JC015587. <https://doi.org/10.1029/2019jc015587>
- Bigorre, S. P., & Plueddemann, A. J. (2021). The annual cycle of air-sea fluxes in the northwest tropical Atlantic. *Frontiers in Marine Science*, 7, 612842. <https://doi.org/10.3389/fmars.2020.612842>
- Blumen, W. (1978). Uniform potential vorticity flow: Part I. theory of wave interactions and two-dimensional turbulence. *Journal of the Atmospheric Sciences*, 35(5), 774–783. [https://doi.org/10.1175/1520-0469\(1978\)035<0774:upvfpj>2.0.co;2](https://doi.org/10.1175/1520-0469(1978)035<0774:upvfpj>2.0.co;2)
- Boccaletti, G., Ferrari, R., & Fox-Kemper, B. (2007). Mixed layer instabilities and restratification. *Journal of Physical Oceanography*, 37(9), 2228–2250. <https://doi.org/10.1175/jpo3101.1>
- Bony, S., & Bjorn, S. (2021). EUREC4a operational center [Dataset]. Retrieved from <https://observations.ipsl.fr/aeris/eurec4a/#/>
- Boutin, J., Chao, Y., Asher, W. E., Delcroix, T., Drucker, R., Drushka, K., et al. (2016). Satellite and in situ salinity: Understanding near-surface stratification and subfootprint variability. *Bulletin of the American Meteorological Society*, 97(8), 1391–1407. <https://doi.org/10.1175/bams-d-15-00032.1>
- Boutin, J., Vergely, J., Reul, N., Catany, R., Koehler, J., & Martin, A. (2021). ESA sea surface salinity climate change initiative (sea_surface_salinity_cci): Weekly and monthly sea surface salinity products, v03. 21, for 2010 to 2020 [Dataset]. *CEDA*. <https://doi.org/10.5285/5920a2c77e3c45339477acd31ce62c3c>
- Boutin, J., Vergely, J.-L., Marchand, S., d'Amico, F., Hasson, A., Kolodziejczyk, N., et al. (2018). New SMOS sea surface salinity with reduced systematic errors and improved variability. *Remote Sensing of Environment*, 214, 115–134. <https://doi.org/10.1016/j.rse.2018.05.022>
- Brannigan, L., Marshall, D. P., Naveira Garabato, A. C., Nurser, A. G., & Kaiser, J. (2017). Submesoscale instabilities in mesoscale eddies. *Journal of Physical Oceanography*, 47(12), 3061–3085. <https://doi.org/10.1175/jpo-d-16-0178.1>
- Callies, J., & Ferrari, R. (2013). Interpreting energy and tracer spectra of upper-ocean turbulence in the submesoscale range (1–200 km). *Journal of Physical Oceanography*, 43(11), 2456–2474. <https://doi.org/10.1175/jpo-d-13-063.1>
- Capet, X., Campos, E., & Paiva, A. (2008). Submesoscale activity over the Argentinian shelf. *Geophysical Research Letters*, 35(15), L15605. <https://doi.org/10.1029/2008gl034736>
- Chapron, B., Kudryavtsev, V., Collard, F., Rasche, N., Kubryakov, A., & Stanichny, S. (2020). Studies of sub-mesoscale variability of the ocean upper layer based on satellite observations data. *Physical Oceanography*, 27(6), 619–630. <https://doi.org/10.22449/1573-160x-2020-6-619-630>
- Charney, J. G. (1971). Geostrophic turbulence. *Journal of the Atmospheric Sciences*, 28(6), 1087–1095. [https://doi.org/10.1175/1520-0469\(1971\)028<1087:gt>2.0.co;2](https://doi.org/10.1175/1520-0469(1971)028<1087:gt>2.0.co;2)
- Chioldi, A. M., Zhang, C., Cokelet, E. D., Yang, Q., Mordy, C. W., Gentemann, C. L., et al. (2021). Exploring the Pacific Arctic seasonal ice zone with Saildrone USVs. *Frontiers in Marine Science*, 8, 640690. <https://doi.org/10.3389/fmars.2021.640690>
- CLS. (2018). Global ocean gridded L4 sea surface heights and derived variables reprocessed 1993 ongoing [Dataset]. <https://doi.org/10.48670/moi-00148>
- Dai, A., & Trenberth, K. E. (2002). Estimates of freshwater discharge from continents: Latitudinal and seasonal variations. *Journal of Hydro-meteorology*, 3(6), 660–687. [https://doi.org/10.1175/1525-7541\(2002\)003<0660:eofdfc>2.0.co;2](https://doi.org/10.1175/1525-7541(2002)003<0660:eofdfc>2.0.co;2)

Acknowledgments

This research has been supported by the European Union Horizon 2020 research and innovation program under grant agreements no. 817578 (TRIATLAS), the Centre National d'Études Spatiales through the BioSWOT and EUREC4A-OA projects, the French national programme LEFE INSU, IFREMER, the French vessel research fleet, the French research infrastructures AERIS and ODATIS, IPSL, the Chaire Chanel programme of the Geosciences Department at ENS and the EUREC4A-OA JPI Ocean and Climate programme. S. Coadou-Chaventon is supported by a Ph.D. grant from ENS Ulm. S. Swart is supported by a Wallenberg Academy Fellowship (WAF 2015.0186), the Swedish Research Council (VR 2019–04400), and the European Unions Horizon 2020 research and innovation programme under Grant 821001 (SO-CHIC). NASA supported the deployment of three SAILDRONES. This publication is also partially funded by the Cooperative Institute for Climate, Ocean, & Ecosystem Studies (CICOES) under NOAA Cooperative Agreement NA20OAR4320271, Contribution No. 2024-1386. This is PMEL contribution No. 5952. We also warmly thank the captain and crew of RVs Atalante, Maria S. Merian, FS Meteor, and Ron Brown. In addition, we gratefully acknowledge the contribution of Dr. Amala Mahadevan for the fruitful discussions.

- de Boyer Montégut, C., Madec, G., Fischer, A. S., Lazar, A., & Iudicone, D. (2004). Mixed layer depth over the global ocean: An examination of profile data and a profile-based climatology. *Journal of Geophysical Research*, 109(C12), C12003. <https://doi.org/10.1029/2004jc002378>
- Dong, J., & Zhong, Y. (2020). Submesoscale fronts observed by satellites over the northern South China Sea shelf. *Dynamics of Atmospheres and Oceans*, 91, 101161. <https://doi.org/10.1016/j.dyatmoce.2020.101161>
- Du Plessis, M., Swart, S., Anson, I., & Mahadevan, A. (2017). Submesoscale processes promote seasonal restratification in the subantarctic ocean. *Journal of Geophysical Research: Oceans*, 122(4), 2960–2975. <https://doi.org/10.1002/2016jc012494>
- Du Plessis, M., Swart, S., Anson, I. J., Mahadevan, A., & Thompson, A. F. (2019). Southern ocean seasonal restratification delayed by submesoscale wind–front interactions. *Journal of Physical Oceanography*, 49(4), 1035–1053. <https://doi.org/10.1175/jpo-d-18-0136.1>
- Fernández, P., Speich, S., Borgnino, M., Meroni, A. N., Desbiolles, F., & Pasquero, C. (2023). On the importance of the atmospheric coupling to the small-scale ocean in the modulation of latent heat flux. *Frontiers in Marine Science*, 10, 1136558. <https://doi.org/10.3389/fmars.2023.1136558>
- Ffield, A. (2007). Amazon and Orinoco River plumes and NBC rings: Bystanders or participants in hurricane events? *Journal of Climate*, 20(2), 316–333. <https://doi.org/10.1175/jcli3985.1>
- Foltz, G. R., Grodsky, S. A., Carton, J. A., & McPhaden, M. J. (2003). Seasonal mixed layer heat budget of the tropical Atlantic Ocean. *Journal of Geophysical Research*, 108(C5), 3146. <https://doi.org/10.1029/2002jc001584>
- Foltz, G. R., Hummels, R., Dengler, M., Perez, R. C., & Araujo, M. (2020). Vertical turbulent cooling of the mixed layer in the Atlantic ITCZ and trade wind regions. *Journal of Geophysical Research: Oceans*, 125(2), e2019JC015529. <https://doi.org/10.1029/2019jc015529>
- Fournier, S., Vandemark, D., Gaultier, L., Lee, T., Jonsson, B., & Gierach, M. M. (2017). Interannual variation in offshore advection of Amazon–Orinoco plume waters: Observations, forcing mechanisms, and impacts. *Journal of Geophysical Research: Oceans*, 122(11), 8966–8982. <https://doi.org/10.1002/2017jc013103>
- Fox-Kemper, B., Ferrari, R., & Hallberg, R. (2008). Parameterization of mixed layer eddies. Part I: Theory and diagnosis. *Journal of Physical Oceanography*, 38(6), 1145–1165. <https://doi.org/10.1175/2007jpo3792.1>
- Fratantoni, D. M., & Glickson, D. A. (2002). North Brazil Current ring generation and evolution observed with SeaWiFS. *Journal of Physical Oceanography*, 32(3), 1058–1074. [https://doi.org/10.1175/1520-0485\(2002\)032<1058:nbcrga>2.0.co;2](https://doi.org/10.1175/1520-0485(2002)032<1058:nbcrga>2.0.co;2)
- Gamage, N., & Blumen, W. (1993). Comparative analysis of low-level cold fronts: Wavelet, Fourier, and empirical orthogonal function decompositions. *Monthly Weather Review*, 121(10), 2867–2878. [https://doi.org/10.1175/1520-0493\(1993\)121<2867:caollc>2.0.co;2](https://doi.org/10.1175/1520-0493(1993)121<2867:caollc>2.0.co;2)
- Giddy, I., Swart, S., du Plessis, M., Thompson, A. F., & Nicholson, S.-A. (2021). Stirring of sea-ice meltwater enhances submesoscale fronts in the Southern Ocean. *Journal of Geophysical Research: Oceans*, 126(4), e2020JC016814. <https://doi.org/10.1029/2020jc016814>
- Hall, K., Daley, A., Whitehall, S., Sandiford, S., & Gentemann, C. L. (2022). Validating salinity from SMAP and HYCOM data with Saildrone data during EUREC4A-OA/ATOMIC. *Remote Sensing*, 14(14), 3375. <https://doi.org/10.3390/rs14143375>
- Hersbach, H., Bell, B., Berrisford, P., Biavati, G., Horányi, A., Muñoz Sabater, J., et al. (2021). ERA5 hourly data on single levels from 1979 to present. *Copernicus Climate Change Service (C3S) Climate Data Store (CDS)*. [Cited 2021 Oct 29].
- Hewitt, H., Fox-Kemper, B., Pearson, B., Roberts, M., & Klocke, D. (2022). The small scales of the ocean may hold the key to surprises. *Nature Climate Change*, 12(6), 496–499. <https://doi.org/10.1038/s41558-022-01386-6>
- Hu, C., Montgomery, E. T., Schmitt, R. W., & Muller-Karger, F. E. (2004). The dispersal of the Amazon and Orinoco River water in the tropical Atlantic and Caribbean Sea: Observation from space and S-PALACE floats. *Deep Sea Research Part II: Topical Studies in Oceanography*, 51(10–11), 1151–1171. <https://doi.org/10.1016/j.dsr.2004.04.001>
- Johnson, G. C., Schmidtko, S., & Lyman, J. M. (2012). Relative contributions of temperature and salinity to seasonal mixed layer density changes and horizontal density gradients. *Journal of Geophysical Research*, 117(C4), C04015. <https://doi.org/10.1029/2011jc007651>
- Karstensen, J., Lavik, G., Acquistapace, C., Baghen, G., Begler, C., Bendinger, A., et al. (2020). EUREC4A campaign, Cruise No. MSM89, 17. January–20. February 2020, Bridgetown (Barbados)–Bridgetown (Barbados), The ocean mesoscale component in the EUREC4A++ field study.
- Klein, P., & Lapeyre, G. (2009). The oceanic vertical pump induced by mesoscale and submesoscale turbulence. *Annual Review of Marine Science*, 1, 351–375. <https://doi.org/10.1146/annurev.marine.010908.163704>
- Klein, P., Treguier, A.-M., & Hua, B. L. (1998). Three-dimensional stirring of thermohaline fronts. *Journal of Marine Research*, 56(3), 589–612. <https://doi.org/10.1357/002224098765213595>
- Köhler, J., Sena Martins, M., Serra, N., & Stammer, D. (2015). Quality assessment of spaceborne sea surface salinity observations over the northern North Atlantic. *Journal of Geophysical Research: Oceans*, 120(1), 94–112. <https://doi.org/10.1002/2014jc010067>
- Kolodziejczyk, N., Reverdin, G., Boutin, J., & Hernandez, O. (2015). Observation of the surface horizontal thermohaline variability at mesoscale to submesoscale in the north-eastern subtropical Atlantic Ocean. *Journal of Geophysical Research: Oceans*, 120(4), 2588–2600. <https://doi.org/10.1002/2014jc010455>
- Lapeyre, G. (2017). Surface quasi-geostrophy. *Fluids*, 2(1), 7. <https://doi.org/10.3390/fluids2010007>
- Laxenaire, R., Speich, S., Blanke, B., Chaigneau, A., Pegliasco, C., & Stegner, A. (2018). Anticyclonic eddies connecting the western boundaries of Indian and Atlantic Oceans. *Journal of Geophysical Research: Oceans*, 123(11), 7651–7677. <https://doi.org/10.1029/2018jc014270>
- Lentz, S. J., & Limeburner, R. (1995). The Amazon River Plume during AMASSEDS: Spatial characteristics and salinity variability. *Journal of Geophysical Research*, 100(C2), 2355–2375. <https://doi.org/10.1029/94jc01411>
- Lévy, M., Ferrari, R., Franks, P. J., Martin, A. P., & Rivière, P. (2012). Bringing physics to life at the submesoscale. *Geophysical Research Letters*, 39(14), L14602. <https://doi.org/10.1029/2012gl052756>
- L'Hégaret, P., Schütte, F., Speich, S., Reverdin, G., Baranowski, D. B., Czeschel, R., et al. (2023). Ocean cross-validated observations from R/Vs L'Atalante, Maria S. Merian, and Meteor and related platforms as part of the EUREC4A-OA/ATOMIC campaign. *Earth System Science Data*, 15(4), 1801–1830. <https://doi.org/10.5194/essd-15-1801-2023>
- Luo, H., Bracco, A., Cardona, Y., & McWilliams, J. C. (2016). Submesoscale circulation in the northern Gulf of Mexico: Surface processes and the impact of the freshwater river input. *Ocean Modelling*, 101, 68–82. <https://doi.org/10.1016/j.ocemod.2016.03.003>
- Mahadevan, A., D'asaro, E., Lee, C., & Perry, M. J. (2012). Eddy-driven stratification initiates North Atlantic spring phytoplankton blooms. *Science*, 337(6090), 54–58. <https://doi.org/10.1126/science.1218740>
- Manucharyan, G. E., & Thompson, A. F. (2017). Submesoscale sea ice–ocean interactions in marginal ice zones. *Journal of Geophysical Research: Oceans*, 122(12), 9455–9475. <https://doi.org/10.1002/2017jc012895>
- Mauzole, Y. (2022). Objective delineation of persistent SST fronts based on global satellite observations. *Remote Sensing of Environment*, 269, 112798. <https://doi.org/10.1016/j.rse.2021.112798>
- McWilliams, J. C. (2016). Submesoscale currents in the ocean. *Proceedings of the Royal Society A: Mathematical, Physical and Engineering Sciences*, 472(2189), 20160117. <https://doi.org/10.1098/rspa.2016.0117>

- McWilliams, J. C., Molemaker, M., & Olafsdottir, E. (2009). Linear fluctuation growth during frontogenesis. *Journal of Physical Oceanography*, 39(12), 3111–3129. <https://doi.org/10.1175/2009jpo4186.1>
- Mensa, J. A., Garraffo, Z., Griffa, A., Özgökmen, T. M., Haza, A., & Veneziani, M. (2013). Seasonality of the submesoscale dynamics in the Gulf Stream region. *Ocean Dynamics*, 63(8), 923–941. <https://doi.org/10.1007/s10236-013-0633-1>
- Meroni, A. N., Parodi, A., & Pasquero, C. (2018). Role of SST patterns on surface wind modulation of a heavy midlatitude precipitation event. *Journal of Geophysical Research: Atmospheres*, 123(17), 9081–9096. <https://doi.org/10.1029/2018jd028276>
- Mignot, J., Lazar, A., & Lacarra, M. (2012). On the formation of barrier layers and associated vertical temperature inversions: A focus on the northwestern tropical Atlantic. *Journal of Geophysical Research*, 117(C2), C02010. <https://doi.org/10.1029/2011jc007435>
- Monteiro, P. M., Gregor, L., Lévy, M., Maenner, S., Sabine, C. L., & Swart, S. (2015). Intraseasonal variability linked to sampling alias in air-sea CO₂ fluxes in the southern ocean. *Geophysical Research Letters*, 42(20), 8507–8514. <https://doi.org/10.1002/2015gl066009>
- Olivier, L., Boutin, J., Reverdin, G., Lefèvre, N., Landschützer, P., Speich, S., et al. (2022). Wintertime process study of the North Brazil Current rings reveals the region as a larger sink for CO₂ than expected. *Biogeosciences*, 19(12), 2969–2988. <https://doi.org/10.5194/bg-19-2969-2022>
- Prieto, G. A. (2022). The multitaper spectrum analysis package in python. *Seismological Society of America*, 93(3), 1922–1929. <https://doi.org/10.1785/0220210332>
- Quinn, P. K., Thompson, E. J., Coffman, D. J., Baidar, S., Bariteau, L., Bates, T. S., et al. (2021). Measurements from the RV Ronald H. Brown and related platforms as part of the Atlantic tradewind ocean-atmosphere mesoscale interaction campaign (ATOMIC). *Earth System Science Data*, 13(4), 1759–1790. <https://doi.org/10.5194/essd-13-1759-2021>
- Reverdin, G., Olivier, L., Foltz, G., Speich, S., Karstensen, J., Horstmann, J., et al. (2021). Formation and evolution of a freshwater plume in the northwestern tropical Atlantic in February 2020. *Journal of Geophysical Research: Oceans*, 126(4), e2020JC016981. <https://doi.org/10.1029/2020jc016981>
- Richardson, P. L., Hufford, G. E., Limeburner, R., & Brown, W. S. (1994). North Brazil current retroflection eddies. *Journal of Geophysical Research*, 99(C3), 5081–5093. <https://doi.org/10.1029/93jc03486>
- Richardson, P. L., & Walsh, D. (1986). Mapping climatological seasonal variations of surface currents in the tropical Atlantic using ship drifts. *Journal of Geophysical Research*, 91(C9), 10537–10550. <https://doi.org/10.1029/jc091ic09p10537>
- Rudnick, D. L., & Ferrari, R. (1999). Compensation of horizontal temperature and salinity gradients in the ocean mixed layer. *Science*, 283(5401), 526–529. <https://doi.org/10.1126/science.283.5401.526>
- Rudnick, D. L., & Martin, J. P. (2002). On the horizontal density ratio in the upper ocean. *Dynamics of Atmospheres and Oceans*, 36(1–3), 3–21. [https://doi.org/10.1016/s0377-0265\(02\)00022-2](https://doi.org/10.1016/s0377-0265(02)00022-2)
- Schott, F. A., Fischer, J., & Stramma, L. (1998). Transports and pathways of the upper-layer circulation in the western tropical Atlantic. *Journal of Physical Oceanography*, 28(10), 1904–1928. [https://doi.org/10.1175/1520-0485\(1998\)028<1904:tapotu>2.0.co;2](https://doi.org/10.1175/1520-0485(1998)028<1904:tapotu>2.0.co;2)
- Shcherbina, A. Y., Sundermeyer, M. A., Kunze, E., D'Asaro, E., Badin, G., Birch, D., et al. (2015). The LatMix summer campaign: Submesoscale stirring in the upper ocean. *Bulletin of the American Meteorological Society*, 96(8), 1257–1279. <https://doi.org/10.1175/bams-d-14-00015.1>
- Siegelman, L., Klein, P., Rivière, P., Thompson, A. F., Torres, H. S., Flexas, M., & Menemenlis, D. (2020). Enhanced upward heat transport at deep submesoscale ocean fronts. *Nature Geoscience*, 13(1), 50–55. <https://doi.org/10.1038/s41561-019-0489-1>
- Simpson, J. (1981). The shelf-sea fronts: Implications of their existence and behaviour. *Philosophical Transactions of the Royal Society of London—Series A: Mathematical and Physical Sciences*, 302(1472), 531–546.
- Small, R. D., de Szoeke, S. P., Xie, S., O'Neill, L., Seo, H., Song, Q., et al. (2008). Air–sea interaction over ocean fronts and eddies. *Dynamics of Atmospheres and Oceans*, 45(3–4), 274–319. <https://doi.org/10.1016/j.dynatmoe.2008.01.001>
- Smith, K. S., & Ferrari, R. (2009). The production and dissipation of compensated thermohaline variance by mesoscale stirring. *Journal of Physical Oceanography*, 39(10), 2477–2501. <https://doi.org/10.1175/2009jpo4103.1>
- Speich, S., & The Embarked Science Team. (2021). *EUREC4A-OA. Cruise report. 19 January – 19 February 2020. Vessel: L'ATALANTE*. FOF. <https://doi.org/10.13155/80129>
- Spiro Jaeger, G., & Mahadevan, A. (2018). Submesoscale-selective compensation of fronts in a salinity-stratified ocean. *Science Advances*, 4(2), e1701504. <https://doi.org/10.1126/sciadv.1701504>
- Stevens, B., Bony, S., Farrell, D., Ament, F., Blyth, A., Fairall, C., et al. (2021). EUREC4A. *Earth System Science Data Discussions*, 1–78.
- Stum, J., Tebri, H., Lehodey, P., Senina, I., Greiner, E., Lucas, M., & Steinmetz, F. (2015). NRT operational chlorophyll maps calculation for marine applications. In *Poster presented at the 2nd IOCS meeting, San Francisco, CA*.
- Su, Z., Torres, H., Klein, P., Thompson, A. F., Siegelman, L., Wang, J., et al. (2020). High-frequency submesoscale motions enhance the upward vertical heat transport in the global ocean. *Journal of Geophysical Research: Oceans*, 125(9), e2020JC016544. <https://doi.org/10.1029/2020jc016544>
- Swart, S., du Plessis, M. D., Nicholson, S.-A., Monteiro, P. M., Dove, L. A., Thomalla, S., et al. (2023). The southern ocean mixed layer and its boundary fluxes: Fine-scale observational progress and future research priorities. *Philosophical Transactions of the Royal Society A*, 381(2249), 20220058. <https://doi.org/10.1098/rsta.2022.0058>
- Swart, S., du Plessis, M. D., Thompson, A. F., Biddle, L. C., Giddy, I., Linders, T., et al. (2020). Submesoscale fronts in the Antarctic marginal ice zone and their response to wind forcing. *Geophysical Research Letters*, 47(6), e2019GL086649. <https://doi.org/10.1029/2019gl086649>
- Thompson, A. F., Lazar, A., Buckingham, C., Garabato, A. C. N., Damerell, G. M., & Heywood, K. J. (2016). Open-ocean submesoscale motions: A full seasonal cycle of mixed layer instabilities from gliders. *Journal of Physical Oceanography*, 46(4), 1285–1307. <https://doi.org/10.1175/jpo-d-15-0170.1>
- Torrence, C., & Compo, G. P. (1998). A practical guide to wavelet analysis. *Bulletin of the American Meteorological Society*, 79(1), 61–78. [https://doi.org/10.1175/1520-0477\(1998\)079<0061:apgtwa>2.0.co;2](https://doi.org/10.1175/1520-0477(1998)079<0061:apgtwa>2.0.co;2)
- Tozuka, T., & Cronin, M. F. (2014). Role of mixed layer depth in surface frontogenesis: The Agulhas Return Current front. *Geophysical Research Letters*, 41(7), 2447–2453. <https://doi.org/10.1002/2014gl059624>
- Tozuka, T., Cronin, M. F., & Tomita, H. (2017). Surface frontogenesis by surface heat fluxes in the upstream Kuroshio Extension region. *Scientific Reports*, 7(1), 10258. <https://doi.org/10.1038/s41598-017-10268-3>
- Vazquez-Cuervo, J., Gomez-Valdes, J., Bouali, M., Miranda, L. E., Van der Stocken, T., Tang, W., & Gentemann, C. (2019). Using saildrones to validate satellite-derived sea surface salinity and sea surface temperature along the California/Baja Coast. *Remote Sensing*, 11(17), 1964. <https://doi.org/10.3390/rs11171964>
- Wenegrat, J., & Arthur, R. (2018). Response of the atmospheric boundary layer to submesoscale sea surface temperature fronts. *Geophysical Research Letters*, 45(24), 13–505. <https://doi.org/10.1029/2018gl081034>
- Zhang, D., Cronin, M. F., Meinig, C., Farrar, J. T., Jenkins, R., Peacock, D., et al. (2019). Comparing air–sea flux measurements from a new unmanned surface vehicle and proven platforms during the spurs-2 field campaign. *Oceanography*, 32(2), 122–133. <https://doi.org/10.5670/oceanog.2019.220>